Universidad de La Laguna

Facultad de Ciencias
MSc in Astrophysics
2022-23 course
MSc Thesis

Physical parameters of the low-mass eclipsing binary system ASAS J052919-1617.3

Author:
D. Galán Diéguez

Supervisor:
M.J. Arévalo Morales
Departamento de Astrofísica, Universidad de La Laguna
Instituto de Astrofísica de Canarias

Co-supervisor:
R. Iglesias Marzoa
Grupo de Operaciones Telescópicas, Centro de Estudios de Física del Cosmos de Aragón

July 2023

Facultad de Ciencias
MSc in Astrophysics
2022-23 course
MSc Thesis

Physical parameters of the low-mass eclipsing binary system ASAS J052919-1617.3

Author: **Daniel Galán Diéguez**
Departamento de Astrofísica, Universidad de La Laguna
danielgalandieguez.astrofisica@gmail.com

Supervisor: **María Jesús Arévalo Morales**,
Departamento de Astrofísica, Universidad de La Laguna
Instituto de Astrofísica de Canarias
mam@iac.es

Co-supervisor: **Ramón Iglesias Marzoa**,
Grupo de Operaciones Telescópicas, Centro de Estudios de Física del Cosmos de Aragón
riglesias@cefca.es

To my parents Ana and José, and my sister María, I hope you are half as proud as I am of you, because that will already be a lot. To my aunt Belén, for being the person who brought sanity to my disastrous essays. To my grandparents, for being wonderful examples of life. And to my godfather Carlos, whom I love so much.

Thanks to my supervisor María Jesús for her continued dedication, and to my co-supervisor Ramón, not only for instilling in me the passion for binaries, but also for the infinite patience he has had.

I want to end by thanking my friends for all the support they give me, especially Lucía and Boque for putting up with my stress. And I cannot forget those special people who have been with me these two years in Canarias.

"Como no estás experimentado en las cosas del mundo,
todas las cosas que tienen algo de dificultad te parecen imposibles...
Confía en el tiempo que suele dar dulces salidas a muchas
amargas dificultades." - Miguel de Cervantes

Abstract

Context. Low-mass ($M < 1\,M_\odot$) eclipsing binary systems show larger radii and lower effective temperatures than theoretical stellar models predict for isolated stars with the same masses. Eclipsing binaries with low-mass components are hard to find due to their low luminosity. As a consequence, the analysis of the known low-mass eclipsing systems is key to understand this behavior.

Aims. We aim to obtain the physical parameters of the low-mass detached eclipsing binary (LMDEB) ASAS J052919-1617.3, as well as updated ephemeris, and new and more accurate *VRI* light curves (LCs). We also seek to compute a new spectral classification of its components, more precise than those carried out to date.

Methods. For the study of the ASAS J052919-1617.3 system we have carried out photometric observations with the IAC80 telescope of the Observatorio del Teide, and spectroscopic observations with the NOT and INT telescopes of the Observatorio del Roque de los Muchachos.

We have developed a series of automatic `Python` scripts (`BinarAlt`, `PhotoRed`, `AstroNet`, and `BinaPhot`[1]) for the reduction and differential aperture treatment of photometric data; this way, we are able to obtain the light curves of eclipsing binary systems. In addition, NOT grism #17 has been implemented in the `PypeIt` code for the reduction of its spectroscopic data. INT data has been reduced with `PyRAF`.

We computed new ephemeris for the ASAS J052919-1617.3 system using a linear fit to the primary eclipse data. The photometric calibration has been obtained from an automatic script to measure the color indices of the binary system; from them, we calculated the mean $T_{\rm eff}$ in quadrature and at the primary eclipse instant.

The light curves in the *VRI* filters have been analyzed using the `PHOEBE` program, obtaining the physical parameters of ASAS J052919-1617.3 components. We used the spectra of the binary system and the `BINAESPEC` code to obtain the spectral classification of its components.

Results. We present a set of first reliable physical parameters of the ASAS J052919-1617.3 system components, based on *VRI* observations. This system is formed by a primary star of $T_{\rm eff,1} = 5411 \pm 200\,K$, and by a secondary star of $T_{\rm eff,2} = 4695 \pm 200\,K$. We computed a photometric mass ratio $q = 0.8643 \pm 0.0019$ and a circular orbit of inclination $i = 85.657 \pm 0.022$, with no hint of third light.

The spectral classification results in a system form by two stars of G0V and K0V type, or in a G5V-K3V combination (following the possible double classification determined by `BINASPEC`). Both components show signs of activity in the form of emission excess in the H_α line. Our spectral classification clearly differs from that published in the literature (A0V-K1III from Parihar et al., 2009), which is incompatible with the color indices (V-$R_c = 0.451 \pm 0.067$, V-$I_c = 0.878 \pm 0.064$) and the light curves shape computed in this work.

[1] The scripts are available in this repository.

Resumen

Contexto. Los sistemas binarios eclipsantes poco masivos ($M < 1\,M_{\odot}$) presentan mayores radios y menores temperaturas efectivas que los que predicen los modelos teóricos para estrellas aisladas de la misma masa. Las binarias eclipsantes de componentes poco masivas son difíciles de encontrar por su baja luminosidad. Debido a esto, el análisis de sistemas eclipsantes poco masivos es clave para entender su comportamiento físico.

Objetivos. Tenemos como propósito obtener los parámetros físicos de la binaria eclipsante separada de componentes poco masivas (LMDEB) ASAS J052919-1617.3, asi como una actualización de sus efemérides y unas nuevas y más precisas curvas de luz (LCs) en los filtros *VRI*. Buscamos, además, realizar una nueva clasificación espectral de sus componentes, más precisa que las realizadas hasta la fecha.

Métodos. Para el estudio del sistema ASAS J052919-1617.3 hemos realizado observaciones fotométricas en el telescopio IAC80 del Observatorio del Teide y observaciones espectroscópicas en los telescopios NOT e INT del Observatorio del Roque de los Muchachos.

Hemos desarrollado una serie de scripts automáticos en `Python` (`BinarAlt`, `PhotoRed`, `AstroNet`, y `BinaPhot`[2]) para la reducción y tratamiento, mediante apertura diferencial, de datos fotométricos; de esta manera podemos obtener las curvas de luz de sistemas binarios eclipsantes. Además, se ha implementado en el código `PypeIt` el grisma #17 del NOT para la reducción de sus datos espectroscópicos. Los datos del INT han sido reducidos con `PyRAF`.

El cálculo de unas nuevas efemérides para el sistema ASAS J052919-1617.3 se ha realizado a partir de un ajuste lineal a los datos de eclipse primario. La calibración fotométrica se ha obtenido mediante un script automático, con el fin de medir los índices de color del sistema binario; a partir de estos se calcula la $T_{\rm eff}$ media en cuadratura y en el instante de eclipse primario.

Las curvas de luz en los filtros *VRI* se han analizado usando el programa `PHOEBE`, obteniendo los parámetros físicos de las componentes de ASAS J052919-1617.3. Los espectros del sistema binario han sido introducidos en el código `BINAESPEC` para determinar la clasificación espectral de sus componentes.

Resultados. Presentamos el primer conjunto de parámetros físicos de las componentes del sistema ASAS J052919-1617.3, basados en observaciones en los filtros *VRI*. Este sistema está formado por una estrella primaria de $T_{\rm eff,1} = 5411 \pm 200\,$K, y por una estrella secundaria de $T_{\rm eff,2} = 4695 \pm 200\,$, K. Obtenemos una relación de masas fotométrica $q = 0,8643 \pm 0,0019$ y una órbita circular de inclinación $i = 85.657 \pm 0.022$, sin indicios de una tercera luz.

La clasificación espectral proporciona un sistema formado por dos estrellas de tipo G0V y K0V, o una combinación G5V-K3V (siguiendo la posible doble clasificación determinada por `BINASPEC`). Ambas componentes muestran signos de actividad en forma de exceso de emisión en la línea H_{α}. Nuestra clasificación espectral difiere claramente de la publicada en la literatura (A0V-K1III en Parihar et al., 2009), la cúal es incompatible con los índices de color (V-$R_c = 0.451 \pm 0.067$, V-$I_c = 0.878 \pm 0.064$) y la forma de las curvas de luz obtenidos en este trabajo.

[2]Los scripts están disponibles en este repositorio.

Contents

1 Introduction

Many of the stars we observe in the firmament form a physical system, in which two or more orbit around a common center of mass. In fact, it is estimated that less than 50% of the stars are single elements such as the Sun and, at least, 70% of them are low-mass objects, meaning that they have masses below $1\,M_{\odot}$ (Abt, 1983; Pinfield et al., 2003).

Massive stars are intrinsically luminous and can be observed photometrically and spectroscopically in a relatively simple way with telescopes from Earth. As a result there exists, in the literature, a large number of stars from the upper main sequence with their physical parameters well determined (see Torres et al., 2010, for a list of well measured systems).

But the lower main sequence is a entirely different issue, given that its stars are intrinsically faint. Only after the last generation of photometric surveys, databases of low-mass objects has improved; to name one, the All-Sky Automated Survey (ASAS, Pojmanski, 1998) has provided millions of light curves, since its ultimate goal is the detection and investigation of any kind of photometric variability.

Among the different types of binary stars that exist, eclipsing binary systems are particularly interesting: the study of these systems is currently one of the most powerful tools to determine stellar physical parameters. With the photometric light curve (LC) and the radial velocity curve of the eclipsing binary, it is possible to determine, with great precision, the mass and radius of its components; without these type of configuration, determination of said parameters is much more complex.

The study of the new detected low-mass eclipsing binary (LMEB) systems brought to light two main discrepancies with stellar models: from the mass-radius relation, the radii obtained are 10-15% greater than models predict, overcoming the associated uncertainties of the parameters (López-Morales & Ribas, 2005). Also, stars effective temperatures (T_{eff}) are 5-7% lower that models predictions. Therefore, it is important to analyze more LMEB in order to check if these discrepancies between observational results and stellar models are common features or if they are observational sample biases.

ASAS J052919-1617.4 = ASAS 052919-1617.3 = 1RXS J052919.5-161730 (with J2000 equatorial coordinates α = 05:29:19.347, δ = -16:17:18.4) is a LMEB system first published in *The All Sky Automated Survey: Variable Stars in the 0h - 6h Quarter of the Southern Hemisphere* (Pojmanski, 2002). This binary system was an optimal candidate to carry out its study, given that it was classified as detached binary, its magnitude was adequate for observations in the Canary Islands telescopes and its estimated orbital period would allow to obtain, in a few nights, light curves with good orbital phase sampling. In addition, since the related bibliography was limited and incomplete, the study of this binary system was a good opportunity to do an innovative research.

Table 1:
First ASAS J052919-1617.4 observational parameters, published in Szczygieł et al. (2008).

α (J2000)	δ (J2000)	**Period** [d]	**HJD$_0$** [HJD]	***V***	***I*** [3]	**Distance** [pc]
05:29:19.32	-16:17:18.7	0.660855	2451868.72	11.16	10.12	85

Szczygieł et al. (2008) presents a first study of ASAS J052919-1617.4 (Table 1). Their study focuses in making a coronal activity analysis of the sources resulting from combining the ASAS catalog with the ROSAT All Sky Survey (RASS). By using the *V-I* colors, they were able to determine distances and thus bolometric luminosities.

[3] Photometric magnitudes calculated at maximum light.

ASAS J052919-1617.4 is also included in the survey dedicated to the photometry of ROSAT sources (Kiraga, 2012), with light curves in V and I filters (see Figure 1). The last publication that makes reference to our binary system is Cruzalèbes et al. (2019); here only ASAS J052919-1617.4 infrared magnitudes are presented, since no stellar diameters were obtained from its mid-infrarred interferometry.

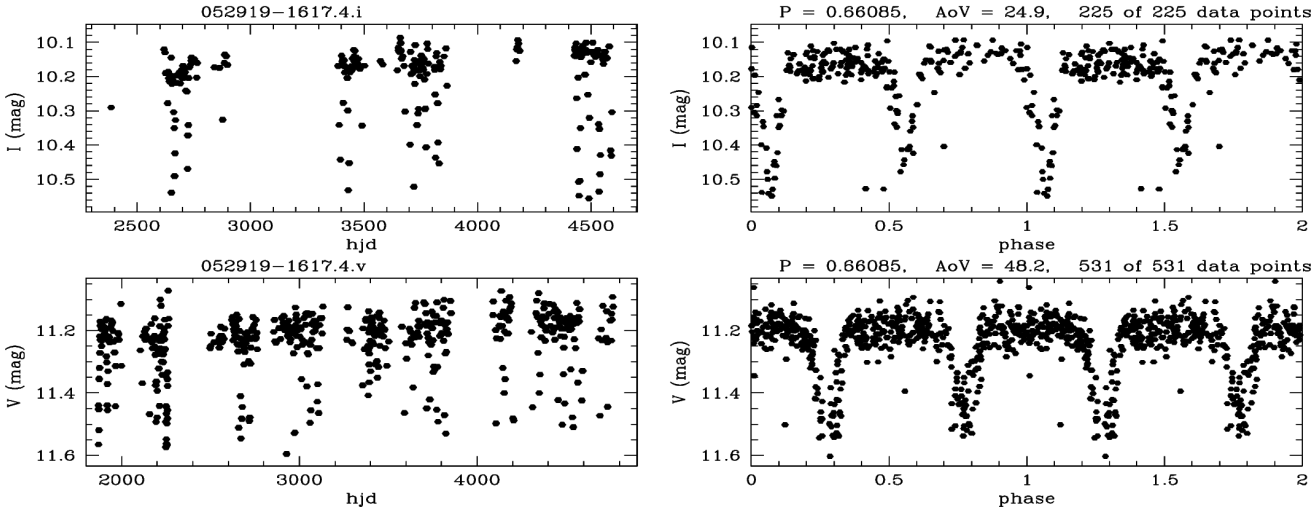

Figure 1: ASAS J052919-1617.3 LCs in the V and I filter, from Kiraga (2012).

The only spectroscopic observations for ASAS J052919-1617.3 are published in Parihar et al. (2009). Using spectra in the H_α region, the authors classified its components as K1III and A0V; as we will discuss in next sections, our results greatly disagree with this classification.

In this work we present new and accurate LCs of ASAS J052919-1617.4 binary system, as well as a more precise orbital period and updated ephemeris. We carried out optical *VRI* band photometric measurements to obtain, not only light curves, but also out-of-eclipse reliable photometric color indices of the system. From the analysis of the LCs, we computed the physical parameters of the ASAS J052919-1617.4 components. Finally, with spectroscopic measurements, we determined their spectral types.

2 Photometric observations

This section details the processes we carried out to work with the photometric data of the binary system ASAS J052919-1617.4, taken at the IAC80 telescope.

First, the design of the observation campaign is described; we developed a new altitude vs time plot script to know which phases are observed during the night. Next, the processes of reduction, astrometrization and adaptive differential photometry are detailed. Here the importance of having developed a set of new scripts for the automatic processing of binary systems photometric data is highlighted.

We discuss the presence of a contaminating star at 3.21 arcsec from ASAS J052919-1617.4, discovered by us and confirmed by Gaia DR3. Finally, the photometric calibration process is presented through our automatic script in `Python`, as well as the uncertainties calculation by Monte Carlo simulations.

2.1 Observation campaign

We used the CAMELOT2 (CAmara MEjorada Ligera del Observatorio del Teide) camera, placed in the IAC80 cassegrain focus and sensitive to the visible range. This CCD has a matrix of 4096x4096 pixels of 15 μm each, providing a pixel scale in the sky of 0.336 arcsec/pixel and a Field of View (FOV) of 23x23 arcmin. CAMELOT2 has 5 readout modes, and we chose mode 1 for the observations. This readout mode allows to obtain an optimal signal-to-noise ratio and deviation from linearity to perform differential photometry, taking into account ASAS J052919-1617.4 V magnitude (see Table 1).

We carried out observations of ASAS J052919-1617.4 with CAMELOT2 during 14 nights, distributed between November 2020 and December 2022, as detailed in Appendix A, Table 12. We used the V, R and I filters of the Johnson-Bessell system, since the purpose of their design allows to measure certain fundamental stellar parameters, such as effective temperatures. So that, physical parameters of the binary system could be obtained from the observations.

2.1.1 Observation schedule

The observation interval of a given celestial body is limited, first, by the date and location of the telescope and, second, by the limitations of the telescope itself. The IAC80 telescope imposes a minimum object altitude of 30° over the horizon for pointing and later observation.

Taking into account these limitations, we developed the `BinarAlt` script with the aim of knowing the position in the sky of any binary system throughout a certain night (see Figure 2). The particularity of this script, and what differentiates it from others available (e.g. Staralt of the Isaac Newton Group of Telescopes), is that it provides information of the orbital phase at every moment of the night (ephemeris available in the AAVSO database were used at this point; see Table 1). So, based on the information provided by this script, we designed the observation program taking into account which phases were approximately covered each night.

At the beginning of each observation night, *bias* and *dome flat-fields* images were acquired; the first ones allow to correct the artificially roughly constant level of counts, while the latter deal with pixel-by-pixel variations in quantum efficiency and non-uniform illumination. Next, the coordinates of ASAS J052919-1617.4 are entered into the telescope system and its tracking is programmed to compensated the rotational movement of Earth. In addition, the FOVIA auto-guiding tool is activated, which detects small tracking

drifts for later corrections using an auxiliary camera and a guide star (easily distinguishable star).

For the ASAS J052919-1617.3 binary system, we set exposure times of 100, 45, 25 seconds for the filters V, R and I respectively. This way, approximately 10,000 counts are secured in each filter, obtaining a reasonable signal-to-noise ratio for photometry. The observation process consisted on observing the 3 filters in sequence, for an adequate temporal sampling.

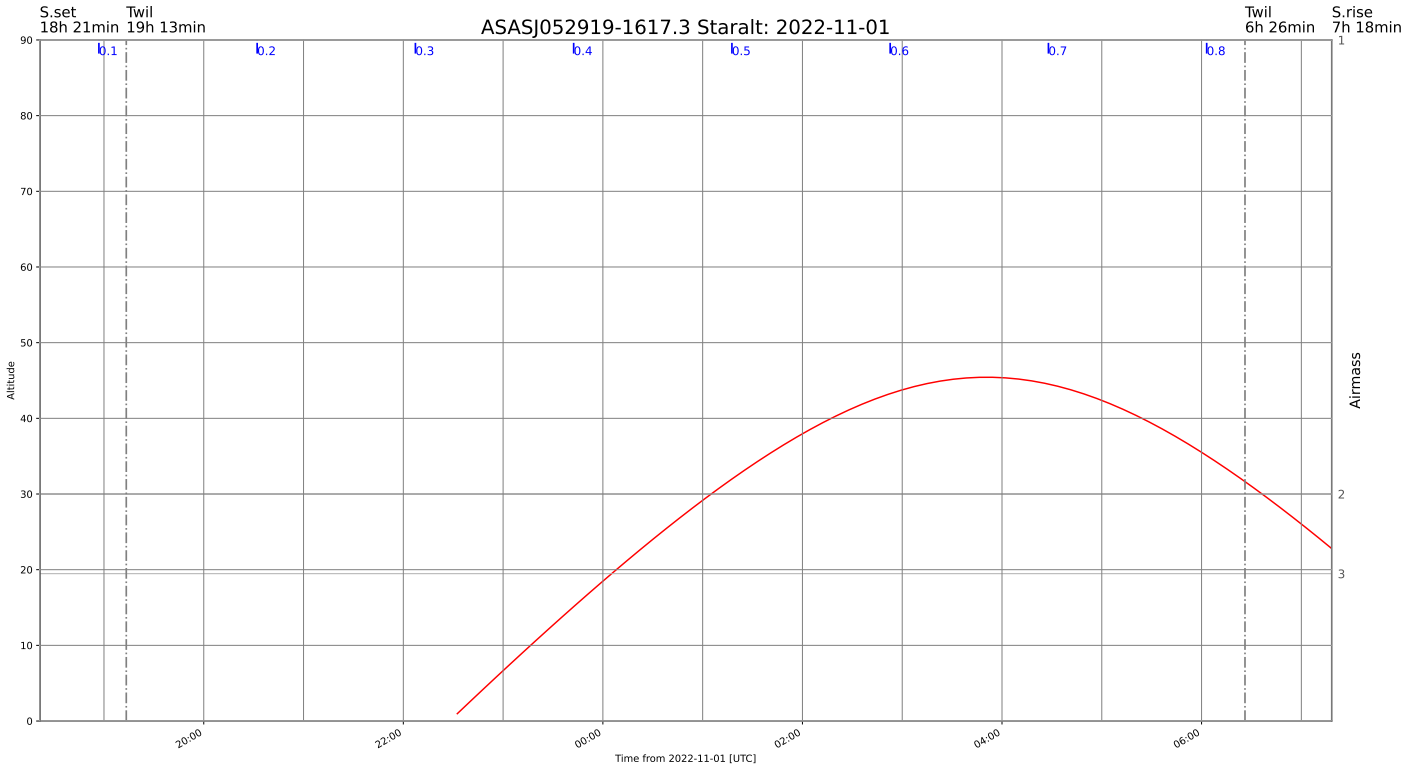

Figure 2: ASAS J052919-1617.4 altitude over the horizon plot for November 1, 2020. The red solid line indicates the sky position of the binary system throughout the night. Vertical dashed lines specify the evening and morning astronomical twilights. Blue ticks at the top of the plot show ASAS J052919-1617.4 orbital phase instants (for their calculation see text).

2.2 Reduction process

The reduction process has been performed with `IRAF` (Image Reduction and Analysis Facility), a collection of software developed by NOAO (National Optical Astronomy Observatory) and dedicated to the processing and analysis of data provided by CCDs (see Tody, 1986, 1993). The reduction tasks have been accessed through the `PyRAF` environment, which allows calling `IRAF` from `Python`.

Telescope images were processed using standard optical reduction techniques which include *bias* subtraction and *flat-field* processing. Mention that, as a result of having recycled the filter wheel of the old IAC80 camera, CAMELOT2 images show significant vignetting: images were trimmed, getting a final FOV of 12x12 arcmin.

Schematically, the reduction process was designed as shown in Figure 3. The *masterbias* was obtained using the task `imcombine`, with a pixels rejection method based on the "minmax" algorithm and with the average as the combination mode. The *masterbias* subtraction from the *flat-field* and the *object* images and their trim was done with `ccdproc`, without taking into account neither the dark current nor the overscan zone (since this zone is not implemented and the dark current is negligible in the CAMELOT2 camera).

On the other hand, the different *masterflats* (one per filter) were obtained with the `flatcombine` task: in this case no rejection method has been applied, since the median is used as the *flat-fields* combination variable [4]; the result of this combination was then normalized using the mean. Finally, each *object* image with the *masterbias* subtracted was divided by its corresponding masterflat.

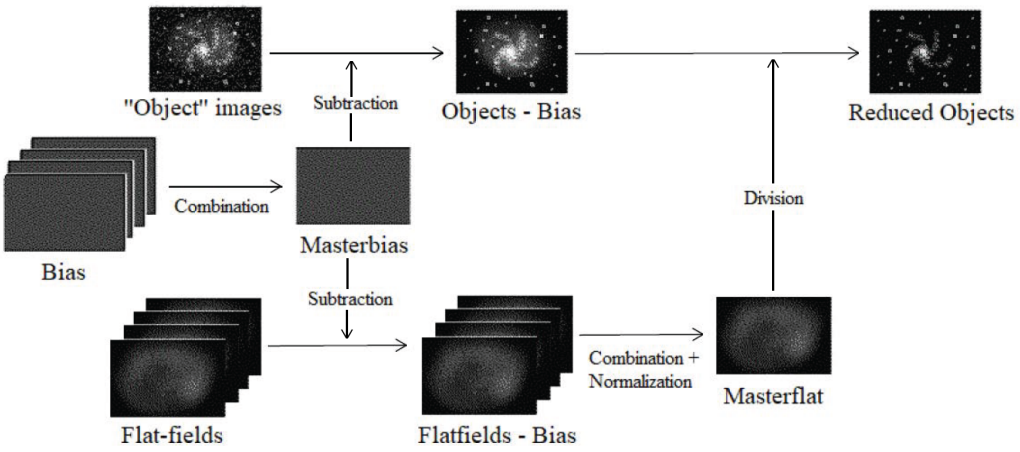

Figure 3: Scheme of the photometric data reduction process.

We have developed the `PhotoRed` script to perform the reduction process. This script has been designed to fit any telescope and set of filters: using an input .json file containing specific information about the telescope (see Appendix B for an example), the script will automatically perform the reduction.

2.3 Astrometrization process

Despite having configured the telescope to compensate Earth's rotation and system drifts in pointing, it is necessary to map the *object* images to obtain a relationship between celestial coordinates and the position (x,y) of each image pixel.

To perform the astrometry, we have developed the `AstroNet` script using two different tasks: `starfind` and `Astrometry.net` (Lang et al., 2010). The first one automatically locates the stars present in the images as well as their position (x,y) and instrumental magnitude. Two critical parameters in this task must be taken into account:

- To determine the detection threshold, 3 times the standard deviation of the sky signal is taken. This ensures to detect stars within within a 99% confidence interval above background noise.
- `Starfind` requires an initial FWHM (Full Width at Half Maximum) value, used to analyze the celestial objects on the image. To determine it, the first taken image in each filter is analyzed using the `imexam` tool: in an arbitrary way, radial profile fits of unsaturated stars are performed, and an average FWHM is calculated from the values measured.

[4] The median is a very illustrative statistic of the pixel counts distribution. It allows to reject cosmic rays, hot pixels, and stars that may appear in each *flat-field*.

Once the stars of the *object* image have been located and ordered by magnitude, a list is created and used by the `Astrometry.net` task to perform the astrometry. This list of stars is used to generate all the possible triangles that can be formed, and then these are compared with those generated from different star catalogs; the matching triangles allow to generate a transformation function between pixel position (x,y) and equatorial coordinates.

Finally, the astrometry world coordinate system (WCS) returned by `Astrometry.net` is saved in the image header.

2.4 Differential aperture photometry

2.4.1 Aperture photometry

Aperture photometry is a technique that takes into account only the number of counts within a specific source-centered aperture, without considering the actual PSF (Point Spread Function) shape of the celestial object.

First, to perform this type of photometry, the PSF center has to be estimated, and then a circular aperture[5] of radius r around that center must be inscribed (Howell, 2006). According to the CCD equation,

$$\mathrm{S/N} = \frac{\mathrm{N_*}}{\sqrt{\mathrm{N_*} + \mathrm{n_{pix}}\left(\mathrm{N_S} + \mathrm{N_D} + \sigma^2_{\mathrm{RON}}\right)}}, \tag{1}$$

to obtain a higher signal-to-noise ratio S/N it is necessary to collect more signal from the source $\mathrm{N_*}$; increasing r up to 3·FWHM, practically 100% of that signal is contained (Figure 4).

In Equation 1 $\mathrm{N_*}$ is the number of photoelectrons produced by the source within the aperture, and $\mathrm{n_{pix}}$ is the number of pixels which form de aperture. Moreover, $\mathrm{N_S}$ and $\mathrm{N_D}$ are the number of electrons per pixel produced by the sky background and the dark current respectively, and σ^2_{RON} is the readout noise ($\mathrm{e^-}$/pixel).

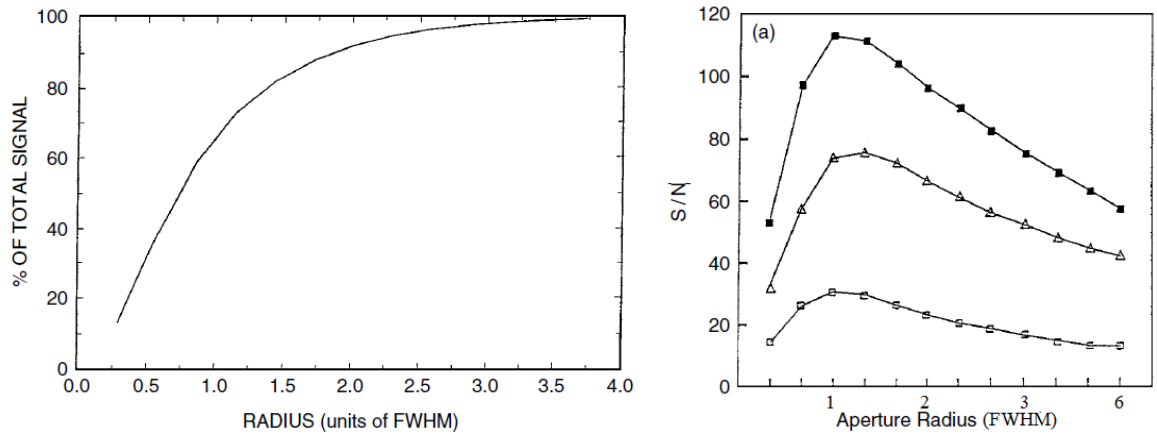

Figure 4: Left: Relationship between the contained source signal and the aperture radius r. Right: Relationship between the signal-to-noise ratio S/N and r; this last plot represents the idea of optimal radius for three point sources that differ in brightness by magnitudes of 0.3 (middle curve) and 2.0 (bottom curve) compared to the top curve (Howell, 2006).

[5]The circular aperture is the usual geometric shape, as it is used for point source photometry.

Moreover, it must be taken into account that the signal collected by the aperture does not correspond exclusively to photons from the analyzed celestial source, but also to photons from the sky background; this additional signal must be estimated and eliminated before performing the photometry. To determine this background level a ring is placed around the aperture, characterized by two variables: the annulus, which corresponds to the inner radius of the ring, and the dannulus, which defines its width. To correctly determine the local background variations, the sky ring must be close to the source without containing any signal from it: the annulus must have a value of about 4· FWHM, as it can be deduced directly from the left subfigure in Figure 4.

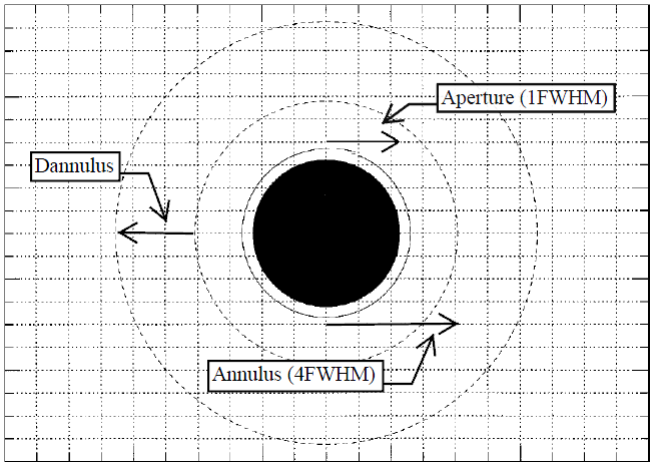

Figure 5: Schematic drawing of a stellar source on a CCD pixel grid (Howell, 2006).

2.4.2 Differential photometry

Differential photometry deals with the measurement of the difference in brightness between astronomical sources that are in the same telescope's FOV; the final result is a relative measurement, since it is only known with respect to other celestial objects. With this type of photometry, the relationship between the sources fluxes is less affected by seeing variations, the atmosphere air mass or the clouds passage: if these elements affect part of the light during an exposure, they will influence by the same fraction in the comparison stars and object fluxes, since they are close together in the sky.

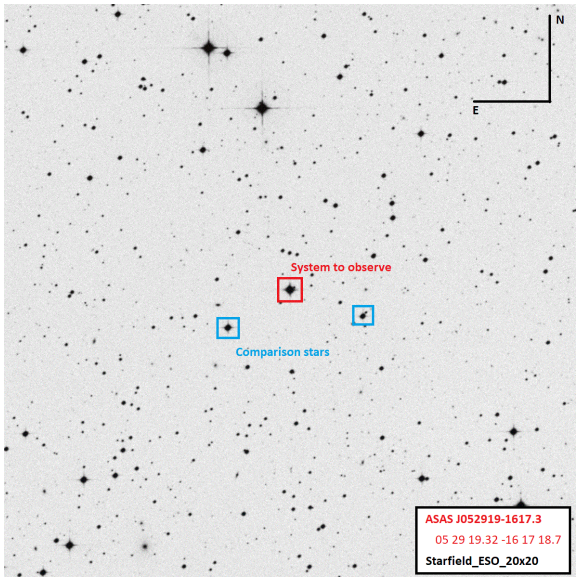

Figure 6: ASAS J052919-1617.3 binary system starfield (ESO Archive, 2022).

To perform aperture differential photometry on ASAS J052919-1617.4 LMEB, we selected two comparison stars (see Table 2 and Figure 6 to know their position in the sky).

Table 2:
Comparison stars for ASAS J052919-1617.3 binary system.

Comparison star ID	α	δ	**Distance to binary system** [arcmin]	**V magnitude**
1	05:29:28.468	-16:18:35.26	2.536	12.27 (0.22)
2	05:29:08.807	-16:18:14.81	2.698	12.44 (0.16)

2.4.3 Adaptative differential aperture photometry process

We have developed `BinaPhot`, an automatic `PyRAF` script to perform differential aperture photometry in any eclipsing binary system. First of all, it is necessary to introduce to the script a series of information about the binary system and its comparison stars, as well as the observatory coordinates where the *object* images were acquired (see Appendix B for a .json file example).

Once the stars of the *object* image have been located (procedure analogous to that described in Section 2.3), the FWHM of each of them is obtained using the `fitpsf` task. The FWHM of the image is calculated using the mode of the `fitpsf` results.

Then, from the FWHM obtained, the parameters of the aperture photometry are defined in `phot`. As indicated in Section 2.4.1 the annulus value is four times the FWHM. The dannulus value has been determined taking into account the signal-to-noise equation (Equation 1): by increasing the ring's width, we would be reducing the error made when estimating the sky background, but not evaluating the local sky. Finally, after different simulations, the dannulus value has been set in such a way that the sky ring has an area two hundred times the aperture area.

The aperture is a completely different issue, and its maximum value is determined by the contaminating star (see Section 2.4.4). Ideally, the aperture radius would be 1·FWHM, but we limited its value to avoid contamination of the external star: the aperture radius oscillates between 3 pixels (in worst seeing cases), and 5 pixels for best seeing situations.

To indicate to `phot` where the binary system and the comparison stars are located in the image, a transformation between their equatorial coordinates and (x,y) image position is necessary. To do so, the `astropy WCS` task uses the transformation function generated by `Astrometry.net`.

When the above values are set, aperture photometry is carried out. The sky background is calculated using the "centroid" algorithm, which uses the mode of the sky pixels histogram (computed using the centroid). This algorithm has been chosen over others because it is reasonably robust in regions with rapidly varying sky backgrounds or populated zones with a high number of stars.

Once the photometry has been performed, `phot` provides the instrumental magnitude m and its associated uncertainty m_{err} for the binary system and its comparison stars through the expressions

$$m_{inst} = m_0 - 2.5 \cdot \log_{10}(F) + 2.5 \cdot \log_{10}(t_{exp}) \quad ; \quad m_{err} = \frac{1}{2}(err_+ + err_-), \tag{2}$$

with

$$F = N - A \cdot m_{sky} \quad ; \quad err_\pm = 2.5 \cdot \log_{10}\left(1 \pm \frac{1}{S/N}\right),$$

where m_0 is the magnitude scale origin, N is the total number of counts in the aperture (including those from the sky background), and A is the aperture area in square pixels. Besides, m_{sky} is the sky background value per pixel, and t_{exp} the exposure time.

Using Equation 2, if m^b_{inst} and m^c_{inst} are the instrumental magnitudes of the binary system and a comparison star respectively, differential photometry gives

$$\Delta m = m^b_{inst} - m^c_{inst} = -2.5 \cdot \log_{10}\left(\frac{F^b}{F^c}\right) \quad ; \quad \Delta m_{err} = \sqrt{(m^b_{err})^2 + (m^c_{err})^2} \tag{3}$$

Finally, since the commonly used date format is not useful for timing astronomical events, the Heliocentric Julian Date (HJD) of each image is calculated. This time format combines the Julian date (number of solar days that have elapsed since 12 UT on January 1, 4713 BC from Greenwich) with a necessary correction to offset the movement of the Earth around the Sun.

HJD time is calculated using the `setjd` task. It uses as time instant half of the exposure time of the *object* image and, as reference, the observatory where the observations were made.

ASAS J052919-1617.4 differential photometry was carried out with `BinaPhot`, using all images in all filters (V, R, I) of the IAC80 telescope. For each comparison star, a set of differential magnitude Δm data is obtained together, with their error and their HJD time.

2.4.4 Contaminating star

The first analysis of ASAS J052919-1617.3 instrumental magnitude variation was made without restriction on the apeture value; that is, the aperture acquired a value that was adapted to the seeing of each image. The obtained LCs presented a series of eruptions without any physical meaning, so a more detailed analysis of the photometric data as well as the available literature was needed.

Firstly, we analyzed the aperture values used in the photometry, verifying that none was high enough to contain star A (Figure 7). Then, we consulted several catalogs both in the infrared (2MASS, AllWise) and optical range (Tycho-2), to verify the existence of a third light or another star; no celestial object in the line of sight of ASAS J052919-1617.3 was found.

Figure 7: Contaminating star identification on the ASAS J052919-1617.3 starfield (ESO Archive, 2022).

The release of Gaia Data Release 3 (Gaia DR3) on June 13, 2022 shed some light on the problem. Given that the spatial resolution of previously consulted catalogues is lower than Gaia DR3, the latter includes celestial bodies that other catalogs were not able to detect. In this way, the suspicion that a star outside the binary system, inside the aperture and not possible to visualize in other catalogs was confirmed.

This contaminating star (star B in Figure 7) is much closer to the binary system than star A (at 3.21 and 10.123 arcsec respectively), and this is the reason why the seeing aperture constraint was not enough to solve the problem. Note that when using an aperture whose value is adapted to the seeing, the flux contribution of the contaminating star was not the same throughout the different days of observation, and even throughout the same night (see Figure 19 to check the seeing evolution throughout the photometric observation nights); this contribution to the aperture counts was not a constant systematic error that would not have affected the shape of the LCs.

According to the information provided by Gaia DR3, said contaminating star presents variability, which we have not confirmed with our photometric observations. To determine the variability of the objects, the DR3 results are based on 34 months of multi-epoch observations, analyzed with statistical and Machine Learning methods to characterize and classify the variable sources (Eyer et al., 2022).

To detect this contaminating star and rule out an unlikely false positive in Gaia data, we used the sCMOS Caronte camera (Cámara de Alta resolución súper Rápida del Observatorio Nocturno del TEide), temporarily installed in the IAC80 telescope. Its spatial resolution of 0.0811 arcsec/pixel and the good seeing of the night allowed us to obtain a clear image of the binary system ASAS J052919-1617.3 and its contaminating star on March 14, 2023 (see Figure 8). To carry out this detection, we discarded the use of lucky imaging instruments, such as FastCam, since the contaminating star is not bright enough.

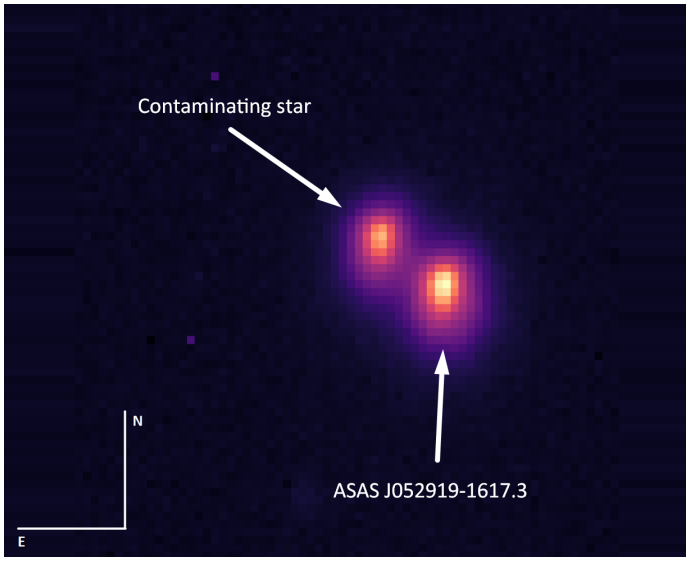

Figure 8: Image in the V filter of ASAS J052919-1617.3 binary system and its contaminating star on March 14, 2023, using the high spatial resolution sCMOS camera Caronte.

In short, to avoid flux contribution from the contaminating star to the ASAS J052919-1617.3 measurements, the value of the aperture was limited according to the day of observation. This values oscillate between 3 pixels (1.008 arcsec, in worst seeing cases), and 5 pixels for best seeing situations (1.66 arcsec).

2.5 Photometric calibration

In general, radiation measurements of celestial objects are made over a limited spectral region using filters. A filter is fully determined if its transmission profile is known, since the central wavelength, spectral width, and effective wavelength $\lambda_{\rm eff}$ are calculated from said profile.

$\lambda_{\rm eff}$ is a wavelength weighted measurement, that provides the wavelength that in a monochromatic measurement would give the flux that is averaged when a filter with a certain bandpass is used. It can be calculated using the expression

$$\lambda_{\rm eff} = \frac{\int_{\lambda_1}^{\lambda_2} \lambda \cdot {\rm I}_\lambda \cdot {\rm T}_\lambda \, {\rm d}\lambda}{\int_{\lambda_1}^{\lambda_2} {\rm I}_\lambda \cdot {\rm T}_\lambda \, {\rm d}\lambda}, \tag{4}$$

where $\mathrm{T}_\lambda = \mathrm{r}(\lambda) + \sum \mathrm{T_i}(\lambda)$, with $\mathrm{r}(\lambda)$ the spectral response of the detector, and $\mathrm{T_i}$ the transmittance of the atmosphere, the telescope and the filter.

Accordingly, $\lambda_{\rm eff}$ does not depend exclusively on the filter, but on the entire spectral response of the detector-telescope-atmosphere system. Hence, even if filters from a standard system are used, the same $\lambda_{\rm eff}$ is never reproduced; there are differences between observatories in the atmosphere, in the detector, in filters, etc. So star colors (magnitudes) deduced in one observatory are not the same as those measured in another one, and there is, therefore, a need to transform colors to those of the standard system.

2.5.1 Photometric calibration process

To carry out the absolute photometric calibration of ASAS J052919-1617.3, we used different standard stars from the Landolt catalog (Landolt, 2009). We observed these standard stars (detailed in Table 13, Appendix A) throughout the photometric night of December 23, 2022 at different air masses in the V, R, and I filters.

We took a total of 150 measurements of the different standard stars, from we could set a series of equations of the form

$$\mathrm{a}_{0,V} + \mathrm{a}_{1,V} \cdot (V-R)_{\mathrm{c_k}} + \mathrm{a}_{2,V} \cdot \mathrm{X}_{V,\mathrm{c_k}} + \mathrm{a}_{3,V} \cdot \mathrm{X}_{V,\mathrm{c_k}} \cdot (V-R)_{\mathrm{c_k}} = \mathrm{m}^{\rm inst}_{V,\mathrm{c_k}} - V_{\mathrm{c_k}} \tag{5}$$

$$\mathrm{a}_{0,R} + \mathrm{a}_{1,R} \cdot (R-I)_{\mathrm{c_k}} + \mathrm{a}_{2,R} \cdot \mathrm{X}_{R,\mathrm{c_k}} + \mathrm{a}_{3,R} \cdot \mathrm{X}_{R,\mathrm{c_k}} \cdot (R-I)_{\mathrm{c_k}} = \mathrm{m}^{\rm inst}_{R,\mathrm{c_k}} - R_{\mathrm{c_k}} \tag{6}$$

$$\mathrm{a}_{0,I} + \mathrm{a}_{1,I} \cdot (V-I)_{\mathrm{c_k}} + \mathrm{a}_{2,I} \cdot \mathrm{X}_{I,\mathrm{c_k}} + \mathrm{a}_{3,I} \cdot \mathrm{X}_{I,\mathrm{c_k}} \cdot (V-I)_{\mathrm{c_k}} = \mathrm{m}^{\rm inst}_{I,\mathrm{c_k}} - I_{\mathrm{c_k}}. \tag{7}$$

Here, the instrumental magnitudes $\mathrm{m}^{\rm inst}_{\mathrm{c_k}}$ of each measured standard star, $\mathrm{c_k}$, form the right-hand column, and capital letters indicate quantities in the standard system. The coefficients $\mathrm{a_0}$ and $\mathrm{a_1}$ are the constant and color terms respectively, while $\mathrm{a_2}$, $\mathrm{a_3}$ are the first and second order atmospheric extinction coefficients. $\mathrm{X_{c_k}}$ is the airmass value in which the standard star has been measured.

For the V filter we had 50 equations of the style of Equation 5, in which the terms $\mathrm{a_i}$ were unknown and the instrumental magnitudes $\mathrm{m}^{\rm inst}_{\mathrm{V,c_k}}$ were obtained following a procedure analogous to the one detailed in Section 2.4.3 [6]. All these expressions form an overdetermined system of linear equations, that we solved using the Moore–Penrose pseudoinverse method (Barata & Hussein, 2012), an algebraic procedure which allows to compute a "least square best fit" to the system.

[6] The Landolt observing program used a 14.0 arcsec diaphragm to measure colors. Thus, we used an aperture radius of 7 arcsec (21.739 pixels in the IAC80 telescope) to perform the photometry on the standard stars.

From the solution of the overdetermined system of equations, and in a similar way for the rest of the filters, we obtained the photometric calibration constants a_i.

Table 3:
Photometric calibration coefficients for December 23, 2022.

Filter	$\mathbf{a_0}$	$\mathbf{a_1}$	$\mathbf{a_2}$	$\mathbf{a_3}$
V	3.9339 ± 0.0099	-0.057 ± 0.028	0.1000 ± 0.0075	0.097 ± 0.023
R_c	3.7844 ± 0.0096	-0.046 ± 0.030	0.0587 ± 0.0071	0.091 ± 0.024
I_c	3.8545 ± 0.0089	-0.108 ± 0.012	0.0245 ± 0.0068	0.0410 ± 0.0093

2.6 Uncertainty computation: Monte Carlo simulations

The Monte Carlo simulation for uncertainty propagation consists on taking as inputs the uncertainty of each datum and generate new values randomly following a normal probability distribution. Here, the original value is the distribution mean and its associated uncertainty is the standard deviation of said probability distribution.

With these new data, the process by which the physical magnitude is obtained (and for which it is wanted to calculate the uncertainty) is repeated, obtaining a new value. After 10.000 interactions, the error of the physical magnitude is obtained by taking the width of the data distribution (got it in said interactions) as its robust uncertainty.

3 Spectroscopic observations

We present, in this section, the spectroscopic observations carried out in the INT and NOT telescopes.

Firstly, the complications encountered when making the observations of ASAS J052919-1617.3 are detailed, both when scheduling them and due to the presence of the contaminating star. Next, we describe the reduction process of the spectroscopic data, in which we have used `PyRAF` and `PypeIt`; we have updated the last one so it can be used with data from the NOT telescope.

3.1 Observation campaign

We acquired the spectroscopic data throughout 11 nights, distributed between January 2022 and December 2022 (see Table 12, Appendix A), and using two different instruments: ALFOSC (Nordic Optical Telescope, NOT) and IDS (Isaac Newton Telescope, INT).

The Alhambra Faint Object Spectrograph and Camera (ALFOSC) is a modular instrument that can perform both imaging and spectroscopy, mounted at the Cassegrain focus in the NOT telescope. We chose to use its Grism #17, with a resolution of R = 10000 and a wavelength range of $6330 - 6870$Å.

IDS (The Intermediate Dispersion Spectrograph) is a long-slit spectrograph which sits at the Cassegrain focal station in the INT telescope. We used the R900V grating, with a 0.69 Å/pix dispersion, a resolution of R = 3261 and a $5850 - 6650$Å wavelength range.

Table 4:
Observed phases of ASAS J052919-1617.3 binary system in spectroscopic mode.

Instrument	**Night**	**Phase** (mid exposure)
ALFOSC Grism #17	2022/02/14	0.87405 ± 0.00034
	2022/02/15	0.42204 ± 0.00034
	2022/11/14	0.24406 ± 0.00032
	2022/12/02	0.34310 ± 0.00032
		0.55439 ± 0.00032
		0.71106 ± 0.00032
IDS R900V	2022/10/23	0.07119 ± 0.00032
		0.08512 ± 0.00032
		0.10250 ± 0.00032
		0.11693 ± 0.00032
		0.13136 ± 0.00032
		0.14579 ± 0.00032

3.1.1 Observation schedule

ASAS J052919-1617.3 system was in the Spanish observing program, so we could only observed it in CAT service time. Since CAT service has a limited number of nights in which there is a large number of observation proposals, ASAS J052919-1617.3 observations were often limited in terms of the used instrument and the time of night in which they were made.

For the ALFOSC instrument, we adopted 500 s of exposure time, while for IDS it was set to 400 s. This difference is due to the fact that ALFOSC resolution is higher than that achieved with IDS.

3.1.2 Contaminating star

It must be highlighted the fact that in ASAS J052919-1617.3 spectroscopic observations the existence of the contaminating star also affected. It was necessary to abandon the optimal observation configuration and seek a different slit orientation from that of the paralactic angle.

The paralactic angle is especially important due to the problem of differential atmospheric refraction. The atmosphere acts practically as a prism, curving the light rays with an angle that depends slightly on the wavelength; a point source really transforms into a small spectrum, oriented vertically and with the red part down (see Figure 9). For this reason it is important, at least in the case of point objects, to try to observe with the slit oriented as close to the paralactic angle as possible.

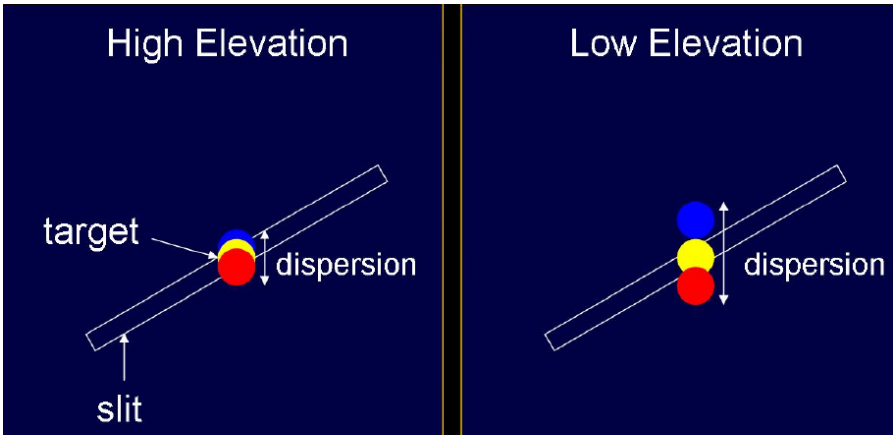

Figure 9: Light loss produced in a slit by differential atmospheric refraction.

However, if the slit were configurated according to the paralactic angle, the traces of the ASAS J052919-1617.3 binary system and the contaminating star would be mixed, affecting the spectra. This way, it was necessary to reach a reasonable commitment between the slit orientation (which did not contain the contaminating star) and the amount of light that was going to be lost, thus increasing the exposure time of the observations.

3.2 Reduction process

3.2.1 NOT telescope

We used the `PypeIt Python` package to reduce ALFOSC spectra (Prochaska et al., 2020a,b; Prochaska et al., 2020c). This package was created for semi-automated reduction of astronomical spectroscopic data and designed to be applied to any standard slit-imaging spectrograph. The use of this package make possible to automate steps in the reduction process (such as wavelength calibration or trace extraction), which otherwise would be tedious when having a considerable amount of spectra.

`PypeIt` requires a configuration file, called the *PypeIt Reduction File*, that has the information about the data (science or calibration file), and how to reduce it (since the reduction process is obviously adapted to the instrument and its configuration). When obtaining our spectroscopic data, ALFOSC Grism #17 was not available in `PypeIt`; we updated the package together with Dr. David Jones (NOT support astronomer) and adapted it to said grism. Currently, when downloading `PypeIt`, Grism #17 data reduction is at hand.

Once the *PypeIt Reduction File* is ready, the package can be executed. It requires no interaction and performs end-to-end data reduction, from calibrations through 2D and 1D spectra for each science frame of ASAS J052919-1617.3 [7].

As the code runs, a series of files are written to the disk. Firts of all, the *masterbias* and the *arc* files created are checked: as typical of most *masterbias* images, it is featureless (effectively noise from the readout), and for the *arc* images one sees a series of arc lines that allow the calibration in wavelength. Also, `PypeIt` also produces *flatfield* images for correcting illumination and pixel-to-pixel variations on the detector.

An example of wavelength calibration is shown in Figure 10. Left subfigure identifies the blue arc lines with green IDs, while the right subfigures correspond to the fit and its corresponding residuals. Moreover, arc lines are traced using a centroid method as a function of spatial position to fit the tilt in the spectral orientation.

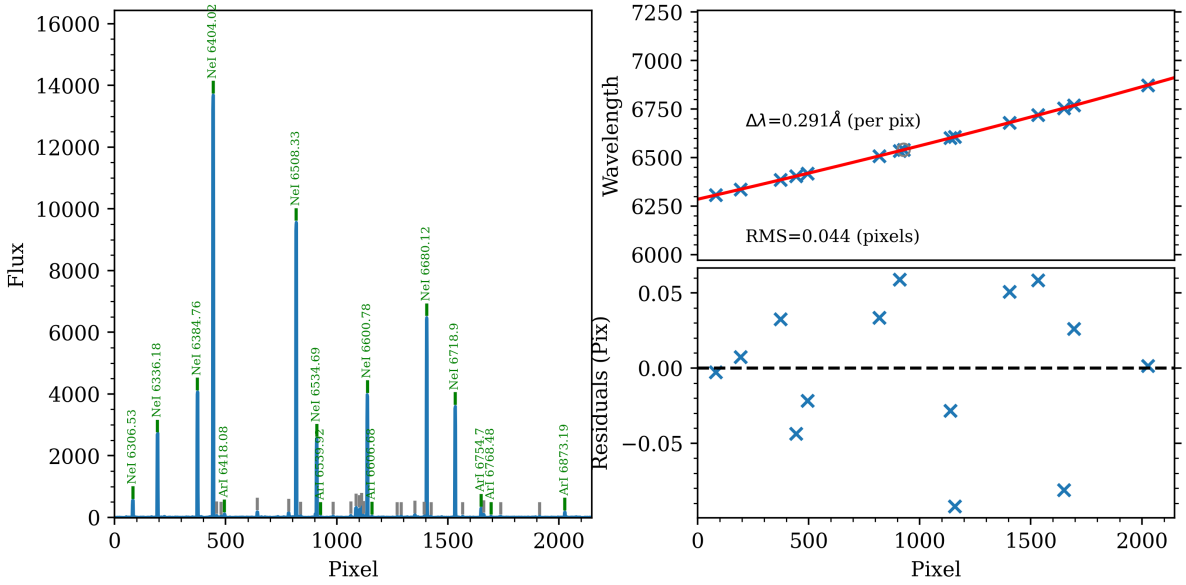

Figure 10: Wavelength calibration fitting results from NOT data on December 02, 2023.

[7] To know more about the reduction process, it is strongly recommended the bibliography available on the `PypeIt` website.

Eventually, the code generates 2D and 1D spectra outputs. In Figure 11, the green lines are the slit edges, and the brighter pixels down the center of the slit are the ASAS J052919-1617.3 spectrum. The line and text in orange color shows the trace and the `PypeIt` assigned name, respectively.

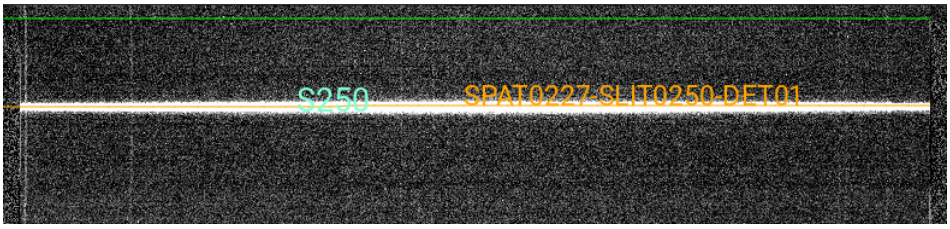

Figure 11: ASAS J052919-1617.3 reduced 2D spectrum using `PypeIt`.

3.2.2 INT telescope

We reduced the IDS spectra following the standard `PyRAF` reduction process. The *masterbias* was obtained using the task `imcombine`, with a pixels rejection method based on the "minmax" algorithm and with the average as the combination mode. The *masterbias* subtraction and trimming from the *flat-field*, *arc* and *object* images was done with `ccdproc`; here we have taken into account, first, the strong vignetting present at the extremes of the spectral range, and the overscan zone (to make up for temporal variations of the bias level).

The *lamp flat-field* images were combined with the `flatcombine` task, using the mean and the "avsigclip" rejection method. We calculated the normalization function with `response`, by the best fit in the spectral direction using Legendre polynomials; the result is a normalized *lamp masterflat*, which allows sensitivity corrections on small scale. The ASAS J052919-1617.3 and *arc* images were divided by this *masterflat*.

The wavelength calibration is done with the `identify` and `reidentify` tasks. The first one allows to link the emission lines of the *arc* images with the ones in the reference spectra. The last task corrects the inclination/curvature of the lines due to flexions in the telescope-spectrograph system. Next, a correlation function between the pixels position (x,y) and λ is obtained using `fitcoords`. With the `transform` task we set the wavelength calibration in ASAS J052919-1617.3 images.

To obtain the binary system flux, we subtracted the sky with the `background` task; the sky around the spectrum is measured from Legendre polynomials of order 3. Finally, the trace was obtained by applying `apall`, thus obtaining the 1D spectrum by summing all the signal in the spatial direction.

To verify that the wavelength calibration came out correctly, we have used the sky emission lines. A first verification consisted of checking their shape; if they are crooked or there is some curvature/inclination, the calibration has not gone completely well. To be more rigorous we carried out gaussian fits to the sky emission lines with `fitprofs`; from the profile center we obtained the position of the lines, having a dispersion, with respect to their position in the laboratory, of less than 5%.

4 Binary system study: PHOEBE and BINAESPEC

In this section we briefly describe the programs we used to study ASAS J052919-1617.3 binary system: the light curves of ASAS J052919-1617.3 have been analyzed with the PHOEBE program, and its spectra with the BINAESPEC code. In this work we only make a brief introduction of them, since there is a large amount of available literature about PHOEBE, and a detailed description of the BINAESPEC code can be found in Section 3 of Lazaro & Arevalo (1997).

4.1 Binary system modelling: PHOEBE

PHysics of Eclipsing BinariEs (PHOEBE) is an open source binary star modelling code (Prša et al., 2016), which reproduces and fits light and radial velocity curves. The code represents a modern implementation of the Wilson-Devinney code (Wilson & Devinney, 1971; Wilson, 1979; Kallrath et al., 1998) with significant refinements, principally with the aim of providing an open, continuously-developed, robust and high-fidelity tool for the modelling of binary stars.

In this work, we used PHOEBE 1.0 (legacy). The procedure carried out to perform the LCs fit consists, first of all, in establishing initial values to the parameters of PHOEBE: some of them will remain fixed (since they are magnitudes that have been obtained by other methods), and others will be fitted until their final value is obtained. In Section 5 we justified the initial parameters values, since in Section 6 the final solution is presented.

4.2 Spectral classification: the BINAESPEC code

To analyze the spectra of the eclipsing binary ASAS J052919-1617.3 we used the BINASPEC code (Lazaro & Arevalo, 1997; Lázaro et al., 2012). This code generates a synthetic spectrum from the spectra combination of two standard stars with short rotational speed, low stellar activity, and solar metallicity (Hoffleit & Jaschek, 1982).

For each observed orbital phase the code produces, in addition to the total synthetic spectrum, those corresponding to each star in the system, scaled in brightness by their contribution to the total spectrum. BINASPEC takes into account rotational broadening and orbital Doppler shift, both in the spectra of the standard stars and in those of the binary system; spectra are corrected for radial velocities. This way, the binary system synthetic spectrum is the sum of the spectra of the primary and secondary components, weighted by their contribution in flux, and Doppler shifted by the appropriate value for the phases of the spectra.

The best fit comes from minimizing the χ^2, difference between the observed spectra and the synthetic spectrum in each orbital phase. When doing the fit, a different weight is given to each phase of the observed spectra, since some are noisier than others.

5 Analysis of the system

We present here a previous analysis of the ASAS J052919-1617.3 system, whose results we used as initial parameters in `PHOEBE` to fit the binary system LCs.

We have obtained, in this section, new ephemeris for ASAS J052919-1617.3, much more precise than those present in the literature. In addition, we present out-of-eclipse photometric color indices, which are used to calculate the mean T_{eff} in quadrature and at the primary eclipse instant. Finally, we make a previous analysis of the ASAS J052919-1617.3 components and its orbital parameters.

5.1 Period and ephemeris

To calculate new ephemeris for ASAS J052919-1617.3, we used the differential magnitudes Δm we had previously obtained. As reference, we selected the comparison star 1 given that its magnitude is closer to ASAS J052919-1617.3 (see Table 2).

To compute the central eclipse instants, we analyzed the eclipse profiles with a least-squares fit (LS) method, using polynomials of degree 3 to 7. We selected the fit degree based on the Bayesian Information Criterion (BIC, Bauldry, 2015), and the minimum of each eclipse is determined from the resulting fit polynomial. Primary eclipses instants of each filter are shown in Table 5, with their uncertainties calculated using Monte Carlo simulations.

Table 5:
ASAS J052919-1617.3 observed primary eclipses instants.

Observation Night	**Filter**	**HJD_{min}** [HJD]
2020/11/01	V	$2459155.643993 \pm 0.000099$
	R	$2459155.64390 \pm 0.00020$
	I	$2459155.64474 \pm 0.00029$
2020/11/03	V	$2459157.62664 \pm 0.00059$
	R	$2459157.62628 \pm 0.00042$
	I	$2459157.62645 \pm 0.00021$
2020/12/28	V	$2459212.47705 \pm 0.00044$
	R	$2459212.47658 \pm 0.00021$
	I	$2459212.47670 \pm 0.00034$
2022/12/15	V	$2459929.50073 \pm 0.00030$
	R	$2459929.50039 \pm 0.00034$
	I	$2459929.50032 \pm 0.00044$

Using a linear ephemeris equation as reference,

$$HJD_{min} = HJD_0 + P \cdot E, \tag{8}$$

we conducted a linear fit to the primary eclipse instants to obtain the period P (Figure 12). Later, we chose the last observed primary eclipse as the ephemeris origin HJD_0 (the mean value of December 15, 2022 data is taken).

As it can be seen from Table 6, when obtaining ASAS J052919-1617.3 ephemeris from IAC80 data, it has been done with greater precision than in the literature; the obtained uncertainties correspond, approximately, to 0.016 s for the period and 18.14 s for HJD_0.

Table 6:
Ephemeris equation parameters of ASAS J052919-1617.3.

Reference	**P** [d]	**HJD$_0$** [HJD]
Szczygieł et al. (2008)	0.660855 ± 0.000010	2451868.720 ± 0.010
This work	$0.66085103 \pm 0.00000018$	$2459929.50048 \pm 0.00021$

The difference between the period published in the AAVSO and the one obtained in this work differ by less than $\approx 0.001\,\%$. However, the accumulation of cycles between the AAVSO ephemeris origin and the observation campaign caused a clear lag between the phases predicted in Section 3.1.1, and those actually observed.

The credibility of the orbital period analysis strictly depends on the correctness of the primary eclipse time determination, as well as on the reliability of its uncertainty estimation. As already specified, we used the LS method to determine the eclipse instants, ruling out a widely used method such as the Kwee-van Woerden method (KWM). This was due to the results published in Mikulášek et al. (2013), which conclude that KWM uncertainties are systematically underestimated.

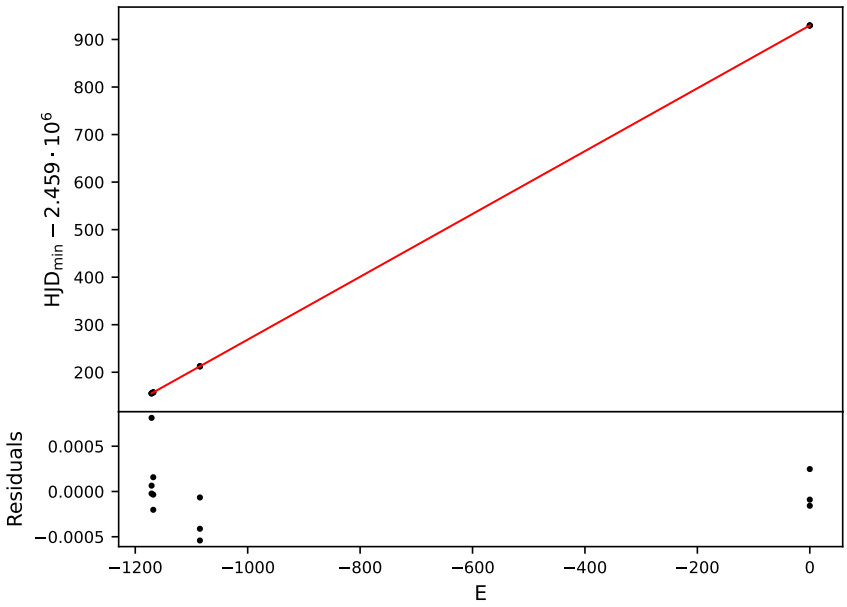

Figure 12: Linear fit to the primary eclipse instants HJD_{min} of ASAS J052919-1617.3. For simplicity time is rescaled, in such a way that the HJD_{min} values shown in the figure are HJD_{min} = HJD_{min} - $2.459 \cdot 10^6$.

We obtained the period P and the HJD_0 value from photometric data of the primary eclipses instants, and not from period estimation algorithms; it can be considered that their values are good enough to not perform a correction in phase. Hence, the phase shift $\Delta\Phi$ parameter is set to zero in the inital `PHOEBE` fit, and only when a first good model was obtained we have freed it to check if its value is compatible with 0 (taking into account the uncertainty).

Also, from the observations, it is not derived that there is a period change with time. Therefore, the period first derivative is set to zero in the fit.

Finally, it is possible to obtain ASAS J052919-1617.3 LCs directly from Equation 8, using that the phase Φ of each magnitude datum is given by the expression

$$\Phi = \mathrm{x} - [\mathrm{x}] \qquad ; \qquad \mathrm{x} = \frac{1}{\mathrm{P}}\,(\mathrm{HJD} - \mathrm{HJD}_0), \tag{9}$$

where [x] is the integer-part function of x.

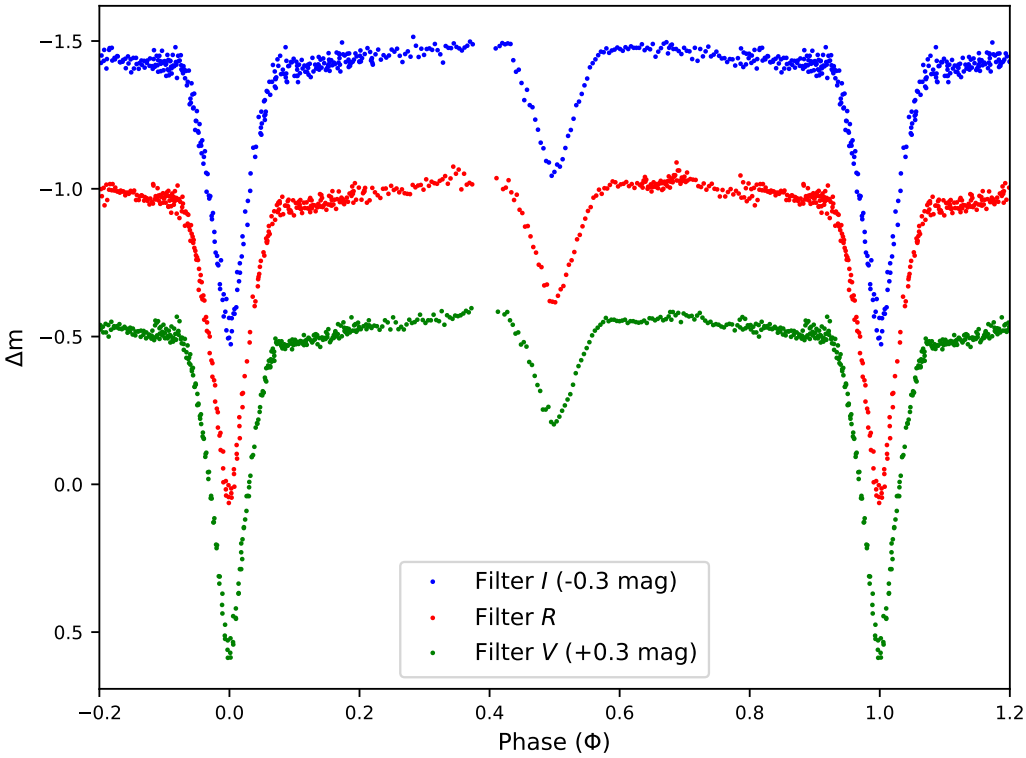

Figure 13: ASAS J052919-1617.3 binary system LCs.

As it can be seen in Figure 13, the ASAS J052919-1617.3 binary system does not present total eclipses, but partial ones. This implies that, from the binary-Earth line of sight, the secondary star is not completely hidden in the secondary eclipse, and in the primary one not all of its surface hides the primary star [8]. Thus, the initial orbit inclination value is set to $i \approx 85°$.

We measured the dispersion at the quadratures in each filter ($\sigma_V = 0.0097$, $\sigma_R = 0.013$, $\sigma_I = 0.013$). These values are used in `PHOEBE` to weight the LCs, giving more importance in the fit to those with less σ (curve-dependent weights).

5.2 Distance and reddening

Dust is composed of heavy elements produced by the nuclear burning on stars. These heavy elements are blown out of the stars in winds and explosions, and are reprocessed in the interstellar medium to eventually form dust grains. Dust scatters and absorbs light, especially in the ultraviolet through infrared range, according to the dust reddening law. Therefore, it is necessary to take this process into account when obtaining calibrated photometry.

[8] We are aware of the ambiguity that exists in the literature regarding the assignment of the role of primary/secondary star in a system. As a criterion, we have used that the primary star is the one hidden in the primary eclipse, and therefore the one with greater surface luminosity.

The Gaia parallax for ASAS J052919-1617.3 is $\pi = 5.975 \pm 0.016$ mas (milli-arcseconds), which translates to a distance of d $= 167.36 \pm 0.45$ pc (Gaia Collaboration et al., 2016, 2022). Galactic reddening maps as Schlafly & Finkbeiner (2011) allowed us to compute a reddening along the binary line of sight of $E(B-V)_\infty = 0.0599 \pm 0.0014$. Said reddening is scaled to the distance d, through the equation

$$E(B-V)_d = E(B-V)_\infty \left[1 - \exp\left(-\frac{|d \cdot \sin b|}{h}\right)\right], \tag{10}$$

where b $= -25.307$ is the Galactic latitude of the binary system, and h is the Galactic scale height taken as h $= 125$ pc (Bahcall & Soneira, 1980); this way, we obtained a value of $E(B-V)_d = 0.02610 \pm 0.00061$.

Table 7:
Calibrated observed magnitudes for ASAS J052919-1617.3 in phase $\Phi = 0.13399 \pm 0.00018$.

Band	Magnitude	Dereddened magnitude
V	11.748 ± 0.048	11.676 ± 0.048
R_c	11.282 ± 0.047	11.225 ± 0.047
I_c	10.837 ± 0.042	10.798 ± 0.042
V-R_c	0.466 ± 0.067	0.451 ± 0.067
V-I_c	0.911 ± 0.064	0.878 ± 0.064
R_c-I_c	0.445 ± 0.063	0.427 ± 0.063

ASAS J052919-1617.3 was observed on December 23, 2022 in phase $\Phi = 0.13399 \pm 0.00018$. Using the photometric calibration coefficients of Table 3 and Equations 5-7, we obtained its calibrated magnitudes (Table 7). Later, we dereddened them using computed interstellar extinctions from the adopted mean value of $E(B-V)_d$ and Table 6 of Schlafly & Finkbeiner (2011) (see Appendix A, Table 14).

5.3 System components

5.3.1 Effective temperatures

To obtain the mean effective temperature of ASAS J052919-1617.3, we used empirical calibrations from Huang et al. (2015), applying FGKM dwarfs coefficients and the dereddened color indices obtained in the previous section. The adopted metallicity for the calibrations is [Fe/H] $= -0.4167 \pm^{0.014}_{0.015}$, iron abundance from GSP-Phot Aeneas best library using BP/RP spectra (Gaia Collaboration et al., 2022).

It seems strange to us that in the solar neighborhood (right in the disc and in a spiral arm) our binary system is so deficient in metallicity, with such small uncertainty. We will discuss this later, in the spectral classification of ASAS J052919-1617.3 (Section 6.2).

The mean T_{eff} value of 5141 ± 180 K (Table 8) is hotter than the spectroscopic value of Gaia DR3 ($4955 \pm^{12}_{15}$ K). Taking into account the uncertainty of both the temperature obtained for the quadrature and that provided by Gaia DR3, it can be assumed that the results are compatible; the different values of T_{eff} have been obtained from different methods (photometry and spectroscopy) and, therefore, a difference of a few hundred kelvins is usual.

Using that

$$\Delta m_{inst} \approx \Delta m_{phot},$$

with m_{inst}, m_{phot} the instrumental and photometric magnitudes respectively, color index values of the primary eclipse can be calculated from

$$m_{phot}\,(\Phi = 0.00) \approx \Delta m_{inst} + m_{phot}\,(\Phi = 0.13),$$

being $\Delta m_{inst} = m_{inst}\,(\Phi = 0.00) - m_{inst}\,(\Phi = 0.13)$. Similarly to the procedure already carried out, we calculated the temperature corresponding to the primary eclipse, obtaining a value of $T_{eff}\,(\Phi = 0.00) = 4827 \pm 180\,K$ (see Table 9).

Table 8:
ASAS J052919-1617.3 mean effective temperature estimations on phase $\Phi = 0.13399 \pm 0.00018$.

Index	**Index value**	$\mathbf{T_{eff}}$ [K]
V-R_c	0.451 ± 0.067	5196 ± 350
V-I_c	0.878 ± 0.064	5132 ± 200
R_c-I_c	0.427 ± 0.063	5093 ± 360
Mean value (adopted)		5141 ± 180

Table 9:
ASAS J052919-1617.3 mean effective temperature estimations on phase $\Phi = 0.0000 \pm 0.0024$.

Index	**Index value**	$\mathbf{T_{eff}}$ [K]
V-R_c	0.505 ± 0.077	4950 ± 350
V-I_c	1.013 ± 0.081	4818 ± 200
R_c-I_c	0.508 ± 0.078	4714 ± 350
Mean value (primary eclipse)		4827 ± 180

The main contribution in quadrature is, approximately, from the primary star, and in the primary eclipse from the secondary star. So, we assumed the primary star initial temperature as $T_{eff,1} = 5141\,K$ and the secondary star initial temperature as $T_{eff,2} = 4827\,K$. Also, their metallicity parameters are fixed to $[Fe/H]_1 = [Fe/H]_2 = -0.4167$.

5.3.2 Surface parameters: potentials, albedo, gravity brightening and reflections

The initial surface potentials of the primary and secondary stars are calculated by `PHOEBE` from the mass ratio, the separation between stars, the star radius (initially assumed to be 1 and $0.5\,R_\odot$) and the synchronicity parameters F_i. We set the albedos to $A_1 = A_2 = 0.5$, following the prescription for stars with convective envelopes from Ruciński (1969).

Gravity brightening β technically varies with the star's temperature roughly as a step function; the strong gradient change occurs when stars goes from a convective to a radiative envelope ($\approx 7000\,K$ on the main sequence). Since the temperatures of the ASAS J052919-1617.3 stars are far from the mentioned strong gradient and they are convective, we fixed the gravity brightening value to $\beta_1 = \beta_2 = 0.32$ (see Claret, 2000).

Finally, we considered that the appropriate number of reflections in the fit was 2; a greater number of reflections would mean a longer computation time without a significant improvement.

5.4 Atmospheres model and limb darkening

The atmospheres of ASAS J052919-1617.3 stars were modeled from Castelli & Kurucz (2003). This atlas contains about 4300 LTE stellar atmosphere models for a wide range of metal abundances, effective temperatures and gravities; these models have no convective overshooting, and they improve opacities and abundances upon previously used by Kurucz (1992).

We selected a square-root limb-darkening law since this is the one that better fits LCs at longer wavelengths (Diaz-Cordoves & Gimenez, 1992; van Hamme, 1993). The limb-darkening coefficients were automatically computed after each iteration using the tables of van Hamme (1993).

5.5 Orbit parameters

5.5.1 Inclination, mass ratio and semimajor axis

Since the LCs of ASAS J052919-1617.3 resemble the one of detached type, the orbital plane is oriented near the line of sight. Taking this into account, we considered that a good starting point is to initially assume an orbital inclination of $i \approx 85°$.

The mass ratio, $q = \frac{M_2}{M_1}$, is obtained from spectroscopy measurements. However, we knew from the beginning that the masses of the ASAS J052919-1617.3 stars were not going to be equal due to their spectral type.

For detached binary systems, the value of q can only be reliably obtained from radial velocity curves; however, it can also be estimated from the LCs by looking which q gives a smaller chi-squared. This last method entails a problem when the eclipses are partial (which is the case of the ASAS J052919-1617.3 system, see Section 5.1): the calculated value may not resemble at all from the one computed with the radial velocities, and therefore, from the real q (see Zhang et al. (2014) and compare their figure 4 with the actual q from Iglesias-Marzoa et al. (2019)).

Despite the previous discussion, since we haven't obtained radial velocity curves for ASAS J052919-1617.3, we decided to start the fit fixing $q = 1$ (being fully aware that it was an erroneous value). Once we got an almost definitive fit model, with the T_{eff} of the system components and using Table 5 of Pecaut & Mamajek (2013), we computed a new mass ratio,

$$q = \frac{0.70\,M_\odot}{0.86\,M_\odot} \approx 0.814. \tag{11}$$

These masses correspond, approximately, to spectral types K1V ($T_{eff,1} = 5141\,K$) and K5V ($T_{eff,2} = 4540\,K$), for solar metallicity. From this moment on, and with this new value, we took q as a free parameter and it was fit with `PHOEBE`.

To determine an approximate value of the semimajor axis a, we used the Kepler's third law,

$$P^2 = \frac{4\pi^2}{G\,(m_1 + m_2)} a^3, \tag{12}$$

with P the orbital period, G the universal gravitational constant, and m_1, m_2 the system components masses. Given the temperatures obtained in Section 5.3.1, m_1, m_2 are approximately 0.86 and $0.78\,M_\odot$ (Pecaut & Mamajek, 2013), obtaining $a \approx 3.765\,R_\odot$, which is the initial value set in `PHOEBE`.

When computing the new value of $q \approx 0.814$, we recalculated the semimajor axis of the system, fixing it at $3.703\,R_\odot$.

5.5.2 Rotation and synchronicity parameters

The secondary eclipse instants for ASAS J052919-1617.3 suggest that the orbit is already circularized, thus the eccentricity $e = 0$ (Table 10). Considering this, and since the synchronicity process is usually faster than the circularization process for convective envelope stars, it is reasonable to assume that the two system components are tidally synchronized (see Hut, 1981). As a result, we fixed the synchronicity parameters to F_1=F_2=1.

Table 10:
ASAS J052919-1617.3 observed secondary eclipses instants.

Observation Night	**Filter**	**HJD$_{\text{secund}}$** [HJD]	**Phase** (mid exposure)
2020/11/02	V	$2459156.63419 \pm 0.00064$	0.4985 ± 0.0011
	R	$2459156.63546 \pm 0.00056$	0.50039 ± 0.00096
	I	$2459156.63495 \pm 0.00094$	0.4996 ± 0.0015

5.5.3 Center-of-mass velocity and argument of periastron.

The center-of-mass velocity γ and the argument of periastron ω are obtained, like q, from the radial velocity curve. Since it is not avaible and it was assumed that $e = 0$, the values of γ and ω were fixed to 0.

5.6 Spot modeling

After making a preliminary fit to the LCs by varying the orbital, system and atmospheric parameters, it was evident the need to include spots in the `PHOEBE` model. This was not surprising, since we were already aware of the very likely existence of spots after obtaining the LCs, and finding that their out-of-eclipses shape was asymmetrical (see Figure 13).

The solid black line in Figure 14 shows a first fit to the LCs without having added spots to ASAS J052919-1617.4 stars. The secondary eclipse is not well fitted, since the model is below the observational data; it is necessary to increase the flux from the binary system model. However, at the exit of the primary eclipse, our model has a higher flux than the data, and hence, it is needed to decrease its superficial luminosity. Note that the preliminary model without spots fits better in the redder filters than in the bluer ones; the spots have less contrast with the photosphere at longer wavelengths.

Since we make the LCs observations for 3 months, it is possible that the spots varied their position and temperature/radius [9]. This variation can be noticed especially at the entrance of the primary eclipse, where there is a small dispersion on the data; given that it seems that the spots evolution is quite stable, we assumed them as static in the fit.

We started by placing two spots on the secondary star: a bright spot ($T_{\text{spot}}/T_{\text{surf}} > 1$) on the secondary eclipse, and a dark one ($T_{\text{spot}}/T_{\text{surf}} < 1$) on the primary eclipse, both facing the observer at said phases; this is equivalent, in `PHOEBE`'s reference system, to placing them at an initial longitude of $\lambda \approx 10, 170°$, respectively. Bearing in mind that the colatitude range most affected by spots on low-mass stars is the equator (Granzer et al., 2000), we began by placing the spots at $\phi \approx 45°$.

[9] Note that the radius and the surface temperature of the spot correlate.

Finally, we allowed to vary the spots parameters (colatitude ϕ, longitude λ, radius r, and temperature ratio T_{spot}/T_{surf}), in order to fit the LCs observed variations.

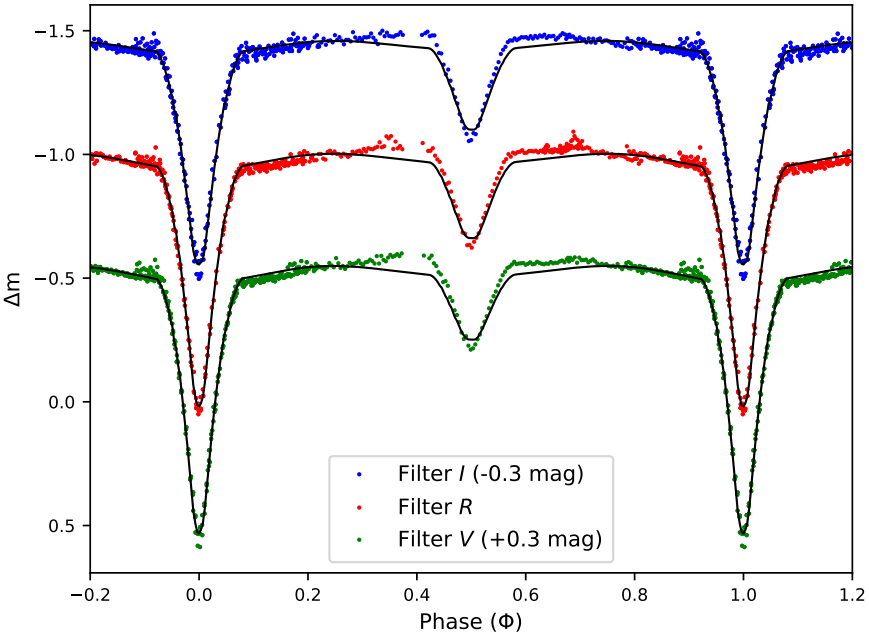

Figure 14: Preliminary fit with no spots (black solid line) to ASAS J052919-1617.3 LCs.

5.7 Third light

A third light, l_3, consists of a contaminant of the binary system, that can be a third component or a field star. This third light is correlated with the orbital inclination, since the eclipse depths of a system with third light can be reproduced with a similar system model but with lower inclination.

Our tests on `PHOEBE` have returned solutions that, in all cases, were compatible with no third light. This is consistent with the RUWE (Renormalized Unit Weight Error) parameter of Gaia DR3, since for ASAS J052919-1617.3 has a value of 0.9991; this variable is expected to be around 1.0 for sources where the single-star model provides a good fit to the astrometric observations.

6 The system of ASAS J052919-1617.4

6.1 Relative parameters

Table 11:
ASAS J052919-1617.4 parameters computed from the best PHOEBE fit to the *VRI* LCs.

Parameter	Primary	Secondary	Parameter	Primary	Secondary
Geometric and orbital parameters			***Luminosities***		
P [d]	$0.66085103 \pm 0.00000018$ [(a)]		$L/(L_1 + L_2)$ [V band]	0.71454 ± 0.00047	0.2855 ± 0.0012
HJD_0 [HJD]	$2459929.50048 \pm 0.00021$ [(a)]		$L/(L_1 + L_2)$ [R band]	0.68506 ± 0.00054	0.3149 ± 0.0012
$\Delta\Phi$	-0.000130 ± 0.000038		$L/(L_1 + L_2)$ [I band]	0.66326 ± 0.00060	0.3367 ± 0.0012
q	0.8643 ± 0.0019		***Limb-darkening coefficients (square-root law)***		
i [deg]	85.657 ± 0.022		x_1, y_1 [bol]	0.379, 0.357	0.485, 0.261
e	0.0 [(a)]		x_1, y_1 [V band]	0.437, 0.375	0.657, 0.170
a [$R_\odot$]	3.703 [(a)]		x_1, y_1 [R band]	0.305, 0.443	0.471, 0.310
ω [deg]	0 [(a)]		x_1, y_1 [I band]	0.194, 0.469	0.310, 0.392
γ [km s^{-1}]	0 [(a)]		***Spot 1 parameters (secondary star)***		
Ω	4.8941 ± 0.0032	4.7628 ± 0.0029	Colatitude ϕ [deg]	-	87.0 ± 1.5
F	1.0 [(a)]	1.0 [(a)]	Longitude λ [deg]	-	9.3 ± 2.2
Radiative parameters			Radius r [deg]	-	34.5 ± 1.6
T_{eff} [K]	5411 ± 200 [(a)]	4695 ± 200	T_{spot}/T_{surf}	-	1.0322 ± 0.0046
A	0.5 [(a)]	0.5 [(a)]	***Spot 2 parameters (secondary star)***		
β	0.32 [(a)]	0.32 [(a)]	Colatitude ϕ [deg]	-	14.6 ± 1.2
l_3 (all bands)	0.0 [(a)]		Longitude λ [deg]	-	166.6 ± 2.5
Fractional radii			Radius r [deg]	-	60.8 ± 1.3
r_{pole}	0.24661 ± 0.00022	0.23229 ± 0.00022	T_{spot}/T_{surf}	-	0.790 ± 0.015
r_{point}	0.25698 ± 0.00028	0.24262 ± 0.00028	***Residuals from the fit***		
r_{side}	0.25017 ± 0.00024	0.23552 ± 0.00024	σ_V [mag]	0.016	
r_{back}	0.25481 ± 0.00027	0.24046 ± 0.00027	σ_R [mag]	0.017	
r_{mn}	0.25214 ± 0.00013	0.23772 ± 0.00013	σ_I [mag]	0.021	

Notes. [(a)]Parameter fixed beforehand.

We fitted the PHOEBE model allowing to vary the following parameters: the phase shift $\Delta\Phi$, the mass ratio q, the orbital inclination i, the secondary effective temperature $T_{eff,2}$, the two surface potentials Ω_1, Ω_2, the passband luminosities (HLA), and the spot parameters (ϕ, λ, r and T_{spot}/T_{surf}).

The parameters obtained for the final solution are shown in Table 11. The uncertainties in this table are the formal ones from the PHOEBE correlation matrix, and they don't include correlations among parameters or systematic effects; the real uncertainties are, almost certainly, greater that the ones of this work. The fitted LCs and their residuals are shown in Figure 15.

The phase shift parameter $\Delta\Phi$ is within 1σ of the HJD_0 value. This confirms the good uncertainty of our ephemeris (Table 6), obtained from the LS method as discussed in Section 5.1.

The computed radii r_i are measured relative to the semimajor axis a, in such a way that the real radii $R_i = r_i \cdot a$; since the value of a has been established in an approximate way in the fit, we cannot accurately compute the absolute radii. We note that the stars are only slightly distorted ($r_{point}/r_{pole} \approx 4.2\,\%$ and $4.4\,\%$ for the primary and secondary star, respectively) in spite of the proximity of the stars ($a = 3.703\,R_\odot$).

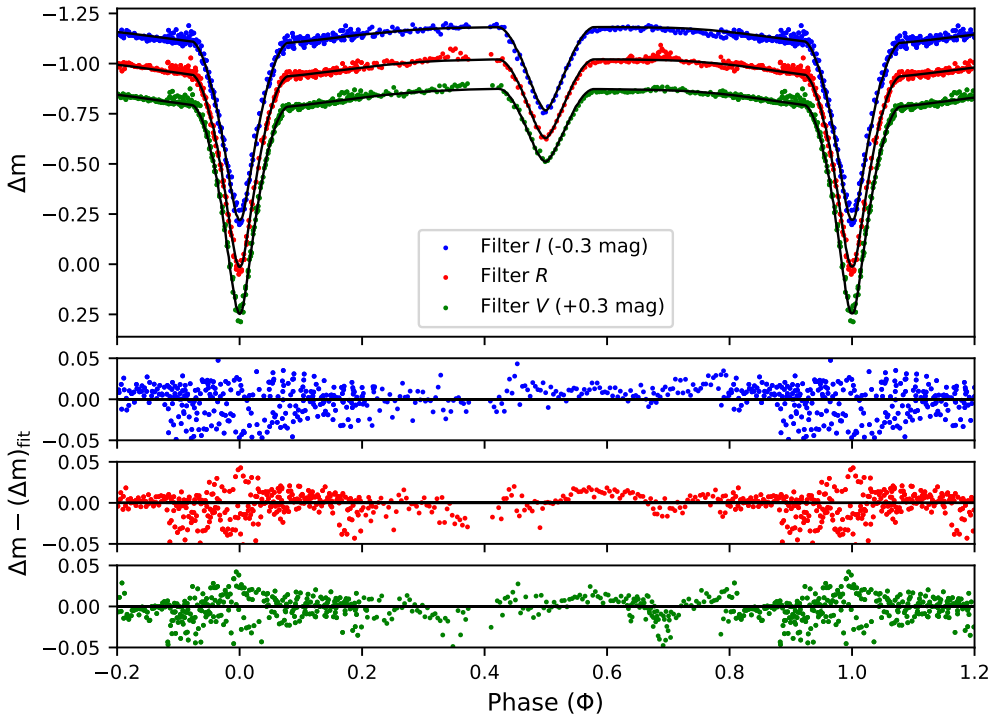

Figure 15: *Top panel*: ASAS J052919-1617.3 LCs (points), and PHOEBE fit model (black solid lines) with the parameters of Table 11. *Lower panels*: residuals of the fits in the same order as the light curves in the top panel.

In Section 5.3.1 we assigned the mean effective temperature of the system to the primary star, so its actual effective temperature must be hotter than the imposed value. To check if the assumed $T_{eff,1}$ should be changed in a new analysis, we estimated the value of $T_{eff,1}$ using the PHOEBE results and the bolometric luminosity equation.

For the system component k we have that $L_k = 4\pi\sigma R_k^2 \cdot T_{eff,k}^4$, and the total bolometric luminosity is $L = L_1 + L_2 = S_T\sigma \cdot T_{eff,mn}^4$. Here S_T is the total surface of the two components, σ the Stefan-Boltzmann constant, and $T_{eff,mn}$ is the mean effective temperature computed from the colors of the system. From these equations we can calculate the $T_{eff,mn}$ using the equation

$$T_{eff,mn} = T_{eff,1}\left[\frac{1 + L_2/L_1}{1 + (L_2/L_1)\,(T_{eff,1}/T_{eff,2})^4}\right]^{1/4}. \quad (13)$$

From the PHOEBE results we computed the L_2/L_1 ratio as

$$\frac{L_2}{L_1} = \frac{R_2^2 \cdot T_{eff,2}^4}{R_1^2 \cdot T_{eff,1}^4} = \frac{r_{vol,2}^2 \cdot T_{eff,2}^4}{r_{vol,1}^2 \cdot T_{eff,1}^4},$$

where $r_{vol,k}$ are the volumetric radii from which the absolute radii can be obtained; we used that $r_{vol,k} \approx r_{mn,k}$, being $r_{mn,k}$ the mean values of the radii $r_{i,k}$ obtained with PHOEBE [10]. Using this approximation in Equation 13 we obtained $T_{eff,1} = 5411 \pm 200$ K, and we fitted again the LCs imposing this corrected $T_{eff,1}$. We recalculated a new $T_{eff,1}$ from the results of the new fit, obtaining $T_{eff,1} = 5442 \pm 200$ K, which is within 1σ

[10] The volumetric radius r_{vol} can be computed solving Equations (1) and (2) of Wilson (1979).

of the first corrected temperature value; we decided to stay with $T_{eff,1} = 5411 \pm 200$ K and with the results of its PHOEBE fit (Table 11).

Figure 16 is a graphical representation of the spots configuration for four orbital phases of ASAS J052919-1617.3 binary system. It is possible that instead of extended spots (34 and 60 degrees), each of them is formed by a group of close smaller spots with higher T_{eff} contrast with the surrounding photosphere, or even that they are spots with variable surface T_{eff} distributions. However, with the data of this work, it is not possible to distinguish among these possibilities; this would require Doppler imaging observations (Strassmeier, 2009).

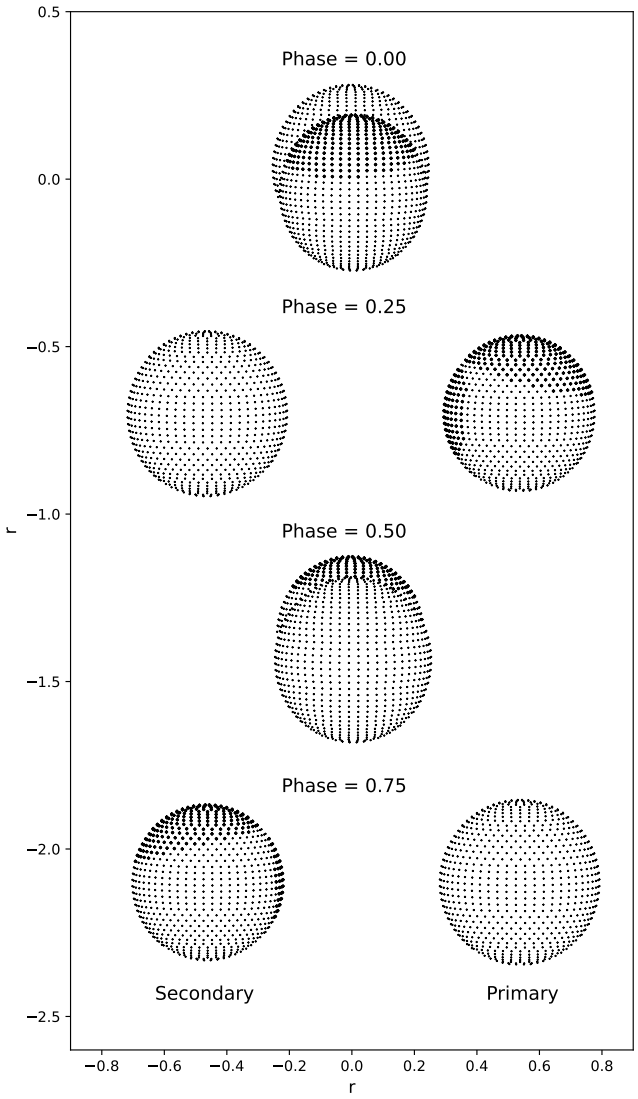

Figure 16: Representation of the spots configuration of ASAS J052919-1617.3 in the (v, w) plane at four phases. From top to bottom: at the primary eclipse (phase 0.0), at the first quadrature (phase 0.25), at the secondary eclipse (phase 0.50), and at the second quadrature (phase 0.75). Both axes have units of relative radius ($r = R/a$) and the images are displaced -0.7 from the previous one. The star in front is orbiting towards the right side and the secondary star is the one with two spots.

In Figure 15, between phases 0.5-0.7, the fit model systematically goes above the photometric points. This may be because we only measured that phase interval once, and PHOEBE gives it less weight in the fit. Another possible explanation is stellar activity or systematics in the photometry in that observation gap. We rule out a spot fit problem since it does not affect a 0.5 phase interval; this fit effect can not be fixed

by adding a new spot, given that spots produce a very wide modulation (almost sinusoidal) and the 0.5-0.7 phase interval is too small.

The physical parameters of this system suggest that the times for the tidal synchronization and orbital circularization are very short (Hut, 1981). Following Hilditch (2001), these times, in units of years, can be computed as

$$t_{sync} \approx 10^4 \left(\frac{1+q}{2 \cdot q}\right)^2 P^4, \tag{14}$$

$$t_{circ} \approx 10^6 \cdot q^{-1} \left(\frac{1+q}{2}\right)^{5/3} P^{16/3}, \tag{15}$$

where $q = \frac{M_2}{M_1}$ is the mass ratio and P is the orbital period in days (both from Table 11). For ASAS J052919-1617.4 these times are $t_{sync} \approx 2 \cdot 10^3$ yr and $t_{circ} \approx 1.1 \cdot 10^5$ yr. Their values are small compared to typical ages of low-mass stars, and justify our assumptions about rotation and synchronicity parameters in Section 5.5.2.

6.2 Spectral classification

The observation and subsequent analysis of the spectra of ASAS J052919-1617.3 binary system has been difficult. ASAS J052919-1617.3 is a relatively weak system with a short orbital period, and exposure times cannot exceed 15 minutes if good orbital phase resolution is desired (good temporal resolution).

At first, our objective was to obtain the radial velocity curve of ASAS J052919-1617.3. To do so, we took spectra with a good temporal sampling, at the cost of losing some signal-to-noise ratio (S/N). The limitations in the observation time, the meteorological conditions, and the presence of the contaminating star in some observations prevented us from obtaining the radial velocity curve.

Despite this setback, and in order to take advantage of the spectra obtained, we decided to carry out the spectral classification of ASAS J052919-1617.3. We note the fact that our spectra were used for a different purpose than the initial one: they have lower S/N than desired for the classification with the `BINASPEC` code (its spectra of standard stars have better S/N than ours).

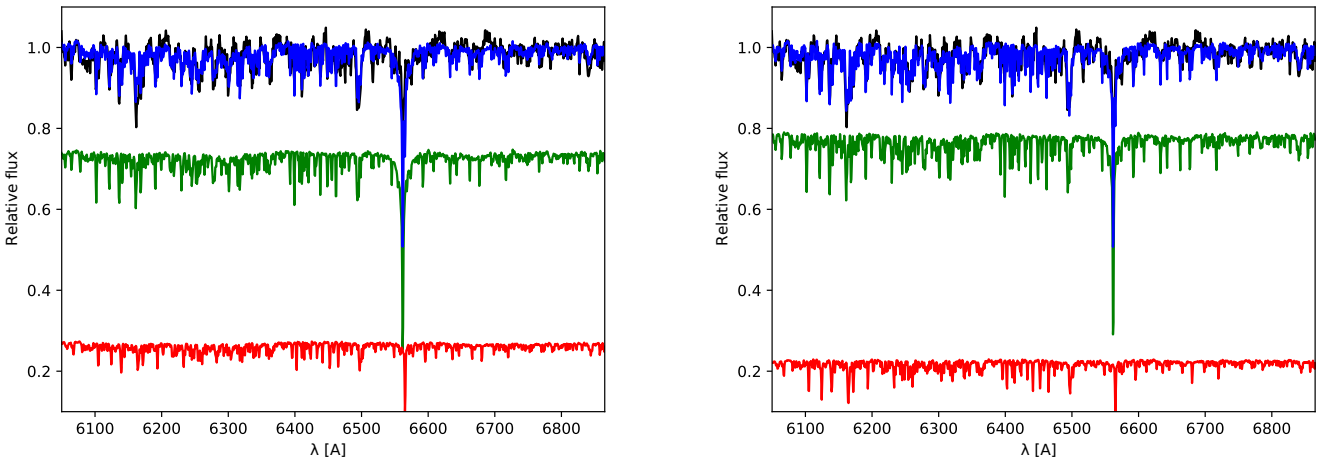

Figure 17: Spectrum of ASAS J052919-1617.3 binary system in phase $\Phi = 0.1025027 \pm 0.00032$ (black). Green and red spectra correspond to the primary and secondary stars in the model, respectively. The blue spectrum is the synthetic spectra of the binary system, combination of the last two spectra and result of the best fit obtained by `BINAESPEC`. From left to right: G0V-K0V and G5V-K3V solutions.

We started the classification with `BINASPEC` from preliminary spectral types. Using Table 5 of Pecaut & Mamajek (2013) and the temperatures of Section 5.3.1 (computed from the quadrature and primary eclipse color indices), we obtained initial spectral types of K1V ($T_{eff,1} = 5141\,K$) and K3V ($T_{eff,2} = 4827\,K$).

The `BINASPEC` code provides two possible solutions: the combinations G5V-K3V and G0V-K0V. With the S/N of our spectra there is no significant difference between both solutions, and the secondary star is poorly determined.

The standard stars used to generate the synthetic spectrum of the binary system are of the type of solar metallicity. From Gaia DR3, ASAS J052919-1617.3 metallicity is $[Fe/H] = -0.4167\pm^{0.014}_{0.015}$ (see Section 5.3.1).

ASAS J052919-1617.3 is a system very deficient in metallicity, something that is rare in the solar neighborhood, right in the disc and in a spiral arm (Lian et al., 2023). Low-mass eclipsing binaries, with short period (less than one day) and synchronized components (orbital and rotation periods equal), have their components rotating at high speed. This causes their lines to be broadened by Doppler effect, which is very difficult to eliminate; if it were possible to measure metallicities, it would be with relatively high uncertainties, and this is not the case for Gaia DR3.

Taking into account this broadening process, that Gaia DR3 uses low-resolution spectra, and the coupling between metallicity and other parameters (such as $\log(g)$ and T_{eff}), we point out that the value $[Fe/H] = -0.4167\pm^{0.014}_{0.015}$ is unreliable. We decided to adopt this value throughout this work, waiting for a more rigorous analysis.

From the effective temperatures resulting from the `PHOEBE` fit (Table 11), we can carry out a spectral classification of the components of ASAS J052919-1617.3. Using again Pecaut & Mamajek (2013), we obtain spectral types G9V ($T_{eff,1} = 5411\,K$) and K4V ($T_{eff,2} = 4695\,K$). This classification is compatible with the `BINAESPEC` results, taking into account the uncertainty with which we worked: both classifications were made from stars with solar metallicity, and our spectra has less S/N than those used by `BINAESPEC`.

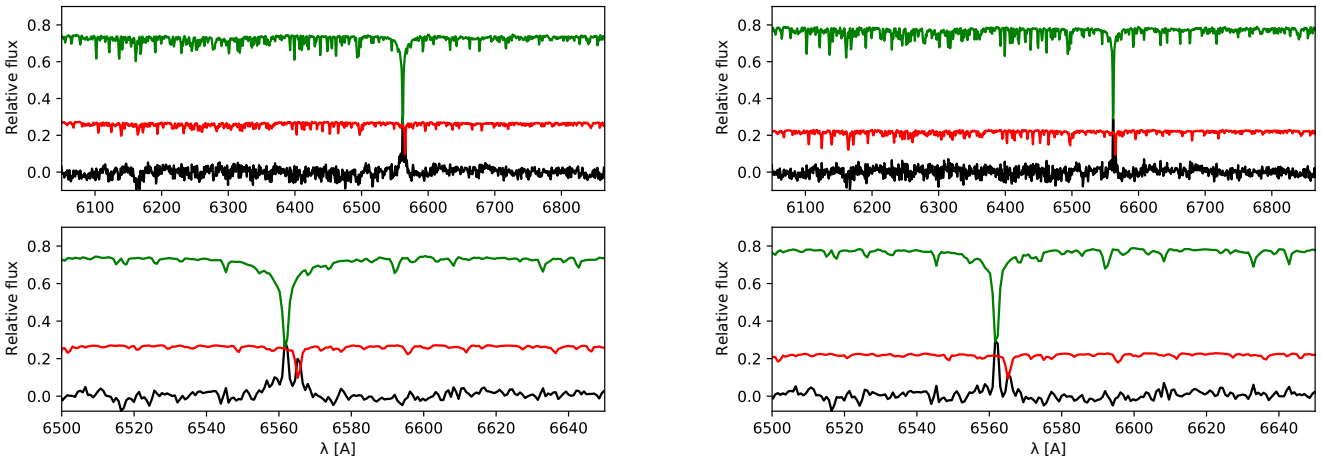

Figure 18: Green model spectra correspond to a G0V (left) and a G5V (right) primary star; red model spectra correspond to a K0V (left) and a K3V (right) secondary star. In black, the residual resulting from subtracting the spectrum of ASAS J052919-1617.3 in phase $\Phi = 0.1025027 \pm 0.00032$ from the synthetic model obtained with `BINAESPEC`.

In Figure 18, once the observed spectrum of ASAS J052919-1617.3 has been subtracted from the synthetic model, it is present an emission excess in the H_α line in both system components. Our spectral classification of ASAS J052919-1617.3 clearly differs from that published in Parihar et al. (2009): they classify the primary star as an A0V type, something that is totally incompatible with the color indices, the LCs shape and the spectra obtained in this work.

7 Conclusions

We present a set of first reliable physical parameters of the ASAS J052919-1617.3 system components based on *VRI* observations. This system is formed by a primary star of $T_{eff,1} = 5411 \pm 200$ K, and by a secondary star of $T_{eff,2} = 4695 \pm 200$ K. We computed a photometric mass ratio $q = 0.8643 \pm 0.0019$ and a circular orbit of $i = 85.657 \pm 0.022$, with no hint of third light.

The spectral classification results in a system form by two stars of G0V and K0V type, or in a G5V-K3V combination (following the possible double classification determined by `BINASPEC`). Both components show signs of activity in the form of emission excess in the H_α line. Our spectral classification clearly differs from that published in the literature (A0V-K1III from Parihar et al., 2009), which is incompatible with the color indices (V-$R_c = 0.451 \pm 0.067$, V-$I_c = 0.878 \pm 0.064$) and the light curves shape computed in this work.

The `Python` scripts developed for this work (`BinarAlt`, `PhotoRed`, `AstroNet`, and `BinaPhot`) are available for the scientific community in this repository. They constitute a set of scripts for observations schedule, photometric data reduction, and automatic LCs computation of eclipsing binary systems.

The work started here is not finished yet, and we consider it a strong basis for future investigations of the ASAS J052919-1617.3 binary system. New observations in the INT, scheduled for the second half of 2023, will allow us to obtain:

- Spectra with good temporal resolution, covering all ASAS J052919-1617.3 phases to obtain its radial velocity curve. With it we could compute reliable mass ratio q and $a \cdot \sin^3(i)$ values, and therefore, the absolute radii and masses of the binary components; we could study the discrepancies between LMEB observational results and stellar models.
- Spectra with a good signal-to-noise ratio to carry out a spectral classification of ASAS J052919-1617.3 components, using stellar atmosphere models and the `BINASPEC` code.
- The origen of the observed stellar activity in ASAS J052919-1617.3, studyinig the emission excess in the H_β line and in the infrared CaII triplet.
- A new metallicity for ASAS J052919-1617.3 from atmosphere models, and comparing it with that provided by Gaia DR3.

References

Abt H. A., 1983, ARA&A, 21, 343

Bahcall J. N., Soneira R. M., 1980, ApJS, 44, 73

Barata J. C. A., Hussein M. S., 2012, Brazilian Journal of Physics, 42, 146

Bauldry S., 2015, in Wright J. D., ed., , International Encyclopedia of the Social Behavioral Sciences (Second Edition), second edition edn, Elsevier, Oxford, pp 615–620, doi:https://doi.org/10.1016/B978-0-08-097086-8.44055-9, https://www.sciencedirect.com/science/article/pii/B9780080970868440559

Castelli F., Kurucz R. L., 2003, in Piskunov N., Weiss W. W., Gray D. F., eds, Vol. 210, Modelling of Stellar Atmospheres. p. A20 (arXiv:astro-ph/0405087), doi:10.48550/arXiv.astro-ph/0405087

Claret A., 2000, A&A, 359, 289

Cruzalèbes P., et al., 2019, MNRAS, 490, 3158

Diaz-Cordoves J., Gimenez A., 1992, A&A, 259, 227

ESO Archive 2022, ESO Online Digitized Sky Survey, http://archive.eso.org/dss/dss

Eyer L., et al., 2022, arXiv e-prints, p. arXiv:2206.06416

Gaia Collaboration et al., 2016, A&A, 595, A1

Gaia Collaboration et al., 2022, arXiv e-prints, p. arXiv:2208.00211

Granzer T., Schüssler M., Caligari P., Strassmeier K. G., 2000, A&A, 355, 1087

Hilditch R. W., 2001, An Introduction to Close Binary Stars

Hoffleit D., Jaschek C., 1982, The Bright Star Catalogue. Fourth revised edition. (Containing data compiled through 1979).

Howell S. B., 2006, Handbook of CCD Astronomy. Vol. 5

Huang Y., Liu X. W., Yuan H. B., Xiang M. S., Chen B. Q., Zhang H. W., 2015, MNRAS, 454, 2863

Hut P., 1981, A&A, 99, 126

Iglesias-Marzoa R., Arévalo M. J., López-Morales M., Torres G., Lázaro C., Coughlin J. L., 2019, A&A, 627, A153

Kallrath J., Milone E., Terrell D., Young A., 1998, The Astrophysical Journal, 508, 308

Kiraga M., 2012, Acta Astron., 62, 67

Kurucz R. L., 1992, in Barbuy B., Renzini A., eds, Vol. 149, The Stellar Populations of Galaxies. p. 225

Landolt A. U., 2009, AJ, 137, 4186

Lang D., Hogg D. W., Mierle K., Blanton M., Roweis S., 2010, AJ, 139, 1782

Lazaro C., Arevalo M. J., 1997, AJ, 113, 2283

Lázaro C., Arévalo M. J., Almenara J. M., Carnerero M. I., Moreno M. A., 2012, New A, 17, 498

Lian J., Bergemann M., Pillepich A., Zasowski G., Lane R. R., 2023, arXiv e-prints, p. arXiv:2306.14100

López-Morales M., Ribas I., 2005, ApJ, 631, 1120

Mikulášek Z., Chrastina M., Zejda M., Janík J., Yhu L., Qian S., 2013, arXiv e-prints, p. arXiv:1311.0207

Parihar P., Messina S., Bama P., Medhi B. J., Muneer S., Velu C., Ahmad A., 2009, MNRAS, 395, 593

Pecaut M. J., Mamajek E. E., 2013, ApJS, 208, 9

Pinfield D. J., Dobbie P. D., Jameson R. F., Steele I. A., Jones H. R. A., Katsiyannis A. C., 2003, MNRAS, 342, 1241

Pojmanski G., 1998, Acta Astron., 48, 35

Pojmanski G., 2002, Acta Astron., 52, 397

Prochaska J. X., et al., 2020a, pypeit/PypeIt: Release 1.0.0, doi:10.5281/zenodo.3743493

Prochaska J. X., Hennawi J. F., Westfall K. B., Cooke R. J., Wang F., Hsyu T., Davies F. B., Farina E. P., 2020b, arXiv e-prints, p. arXiv:2005.06505

Prochaska J. X., et al., 2020c, Journal of Open Source Software, 5, 2308

Prša A., et al., 2016, ApJS, 227, 29

Ruciński S. M., 1969, Acta Astron., 19, 245

Schlafly E. F., Finkbeiner D. P., 2011, ApJ, 737, 103

Strassmeier K. G., 2009, A&A Rev., 17, 251

Szczygieł D. M., Socrates A., Paczyński B., Pojmański G., Pilecki B., 2008, Acta Astron., 58, 405

Tody D., 1986, in Crawford D. L., ed., Society of Photo-Optical Instrumentation Engineers (SPIE) Conference Series Vol. 627, Instrumentation in astronomy VI. p. 733, doi:10.1117/12.968154

Tody D., 1993, in Hanisch R. J., Brissenden R. J. V., Barnes J., eds, Astronomical Society of the Pacific Conference Series Vol. 52, Astronomical Data Analysis Software and Systems II. p. 173

Torres G., Andersen J., Giménez A., 2010, A&A Rev., 18, 67

Wilson R. E., 1979, ApJ, 234, 1054

Wilson R. E., Devinney E. J., 1971, ApJ, 166, 605

Zhang L.-Y., Pi Q.-f., Yang Y.-G., 2014, MNRAS, 442, 2620

van Hamme W., 1993, AJ, 106, 2096

Acknowledgements

- This work is partially based on photometric observations made in the 80cm IAC80 telescope, operated on the Tenerife island by the Instituto de Astrofísica de Canarias (IAC) in the Observatorio del Teide. We thank the staff of Observatorio del Teide, formed by support astronomers (Grupo de Astrónomos de Soporte, GAS), Telescope Observers (TO), telescope operators (Técnico de Operaciones Telescópicas, TOT), and telescopic operations group header, Álex Oscoz Abad.

- We also thank the collaboration of both Dr. David López Fernández-Nespral and Dra. Rosa Clavero Jiménez, for allowing us to make observations with the CARONTE camera, the new high resolution scientific CMOS of the IAC80 telescope.

- Another part of this work is based on observations made in the Observatorios de Canarias del IAC with the 2.56 m Nordic Optical Telescope (NOT) and in the 2.5 m Isaac Newton Telescope (INT), operated on the island of La Palma in the Observatorio del Roque de los Muchachos. The spectroscopic data presented here were partially obtained with ALFOSC, which is provided by the Instituto de Astrofisica de Andalucia (IAA) under a joint agreement with the University of Copenhagen and NOT. Also, we based this work on observations made with the IDS spectrograph at INT under Director's Discretionary Time of Spain's Instituto de Astrofísica de Canarias.

- The observations carried out in the INT and NOT telescopes were possible thanks to the patience and dedication of Dra. Rosa Clavero Jiménez, who assisted us during the observation campaign.

- We thank Dr. David Jones for his great predisposition and help in the implementation of ALFOSC Grism #17 in `PypeIt`.

- Finally, we would like to highlight the collaboration of Dr. Carlos Lázaro Hernando, when it comes to the use of the `BINAESPEC` code.

Appendix A

A.1. Observation nights

Table 12:
Observation nights assigned to the eclipsing binary system ASAS J052919-1617.4.

Telescope	**Mode**	**Instrument**	**Night**	
			[UTC]	[HJD]
IAC80	Photometry	CAMELOT2	2020/11/01	2459155
			2020/11/02	2459156
			2020/11/03	2459157
			2020/11/14 (*)	2459168
			2020/11/15	2459169
			2020/11/19	2459173
			2020/12/03 (*)	2459187
			2020/12/27	2459211
			2020/12/28	2459212
			2021/01/26	2459241
			2021/01/30	2459245
			2021/01/31 (*)	2459246
			2022/12/15	2459929
			2022/12/23	2459937
NOT	Spectroscopy	ALFOSC Grism #17	2022/02/14 (*)	2459625
			2022/02/15	2459626
			2022/10/22 (*)	2459875
			2022/11/14	2459898
			2022/12/02	2459916
INT	Spectroscopy	IDS R900V	2022/02/23	2459634
			2022/10/23 (*)	2459876

Notes. (*) No observations due to weather conditions.

A.2. Seeing evolution in ASAS J052919-1617.3 photometric observations

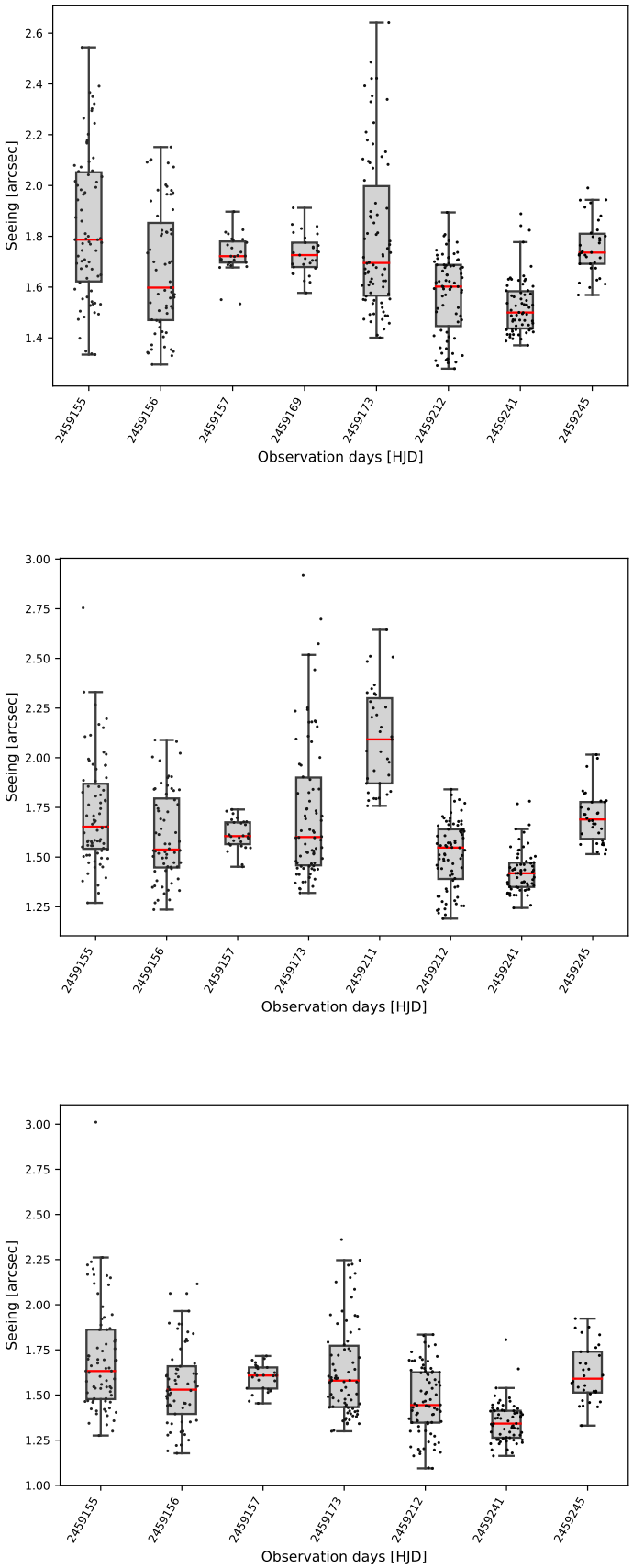

Figure 19: Seeing evolution throughout photometric observation nights of the ASAS J052919-1617.3 binary system. From top to bottom filters V, R, and I. Each box extends from the first quartile (Q1) to the third quartile (Q3) of the data, with a red line at the median. The whiskers extend from the box by 1.5 times the inter-quartile range (IQR). The black scatter points are the observed seeing values.

A.3. Photometic calibrations

Standard Stars

Table 13:
Observed Landolt standard stars to perform photometric calibration (Landolt, 2009)

Standard Star	Coordinates	*V*	*B-V*	*U-B*
Feige 22	02:30:16.627 +05:15:50.70	12.798 ± 0.0009	-0.052 ± 0.0007	-0.809 ± 0.0015
SA 95 236	03:56:13.342 +00:08:47.06	11.487 ± 0.0009	0.737 ± 0.001	0.168 ± 0.0021
PG2317+046	23:19:55.349 +04:52:34.60	12.876 ± 0.0085	-0.246 ± 0.0041	-1.137 ± 0.0079
PG0918+029D	09:21:21.936 +02:47:28.28	12.272 ± 0.0021	1.044 ± 0.003	0.821 ± 0.0071
GD 71	05:52:27.619 +15:53:13.23	13.033 ± 0.0011	-0.248 ± 0.0009	-1.11 ± 0.001

Standard Star	*V-R*	*R-I*	*V-I*
Feige 22	-0.103 ± 0.0007	-0.105 ± 0.0013	-0.206 ± 0.0013
SA 95 236	0.419 ± 0.0008	0.412 ± 0.0004	0.831 ± 0.001
PG2317+046	-0.074 ± 0.0032	-0.035 ± 0.0028	-0.118 ± 0.0079
PG0918+029D	0.575 ± 0.0016	0.535 ± 0.0018	1.108 ± 0.0018
GD 71	-0.138 ± 0.0009	-0.166 ± 0.0017	-0.304 ± 0.0021

Extinction coefficients

Table 14:
Extinction coefficients from Schlafly & Finkbeiner (2011), with $\mathrm{E}(B-V)_\mathrm{d}$=$0.02610 \pm 0.00061$.

Filter	$\mathrm{A_i}/\mathrm{E}(B-V)$	$\mathrm{A_i}$
V	2.742	0.0716 ± 0.0017
R	2.169	0.0566 ± 0.0013
I	1.505	0.03928 ± 0.00092

Calibration constants residuals

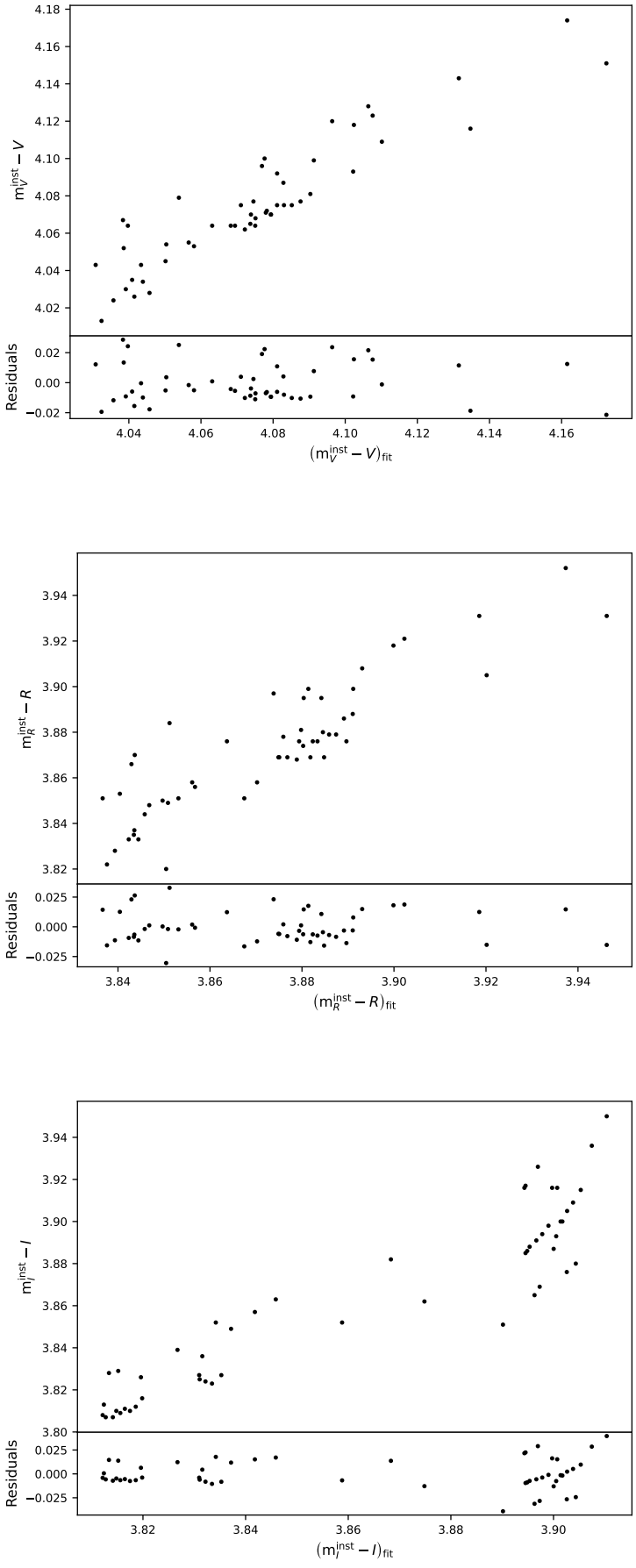

Figure 20: Residuals from the photometric calibration coefficients calculation for the filters V (top), R (middle) and I (bottom).

Appendix B

IAC80 telescope configuration file (Mode 1)


```
[
 {
 "telescope": "IAC80",

 "observatoryname_header": "OBSERVAT",
 "observatory": "OT",

 "x_1": 1000,
 "x_2": 3096,
 "y_1": 1000,
 "y_2": 3112,

 "X_1": 1,
 "X_2": 1,
 "Y_1": 1,
 "Y_2": 1,

 "dateobsname_header": "DATE-OBS",
 "epochname_header": "EPOCH",
 "hjdname_header": "HJD",
 "jdname_header": "JD",

 "typefits_header": "IMAGETYP",
 "typefits_bias_header": "BIAS",
 "typefits_flat_header": "FLAT",
 "typefits_object_header": "OBJECT",

 "filtername_header": "INSFILTE",

 "exposuretimename_header": "EXPTIME",

 "airmassname_header": "AIRMASS",

 "saturationname_header": "SATURATION",
 "saturation": 56000,

 "gainname_header": "GAIN",
 "gain": 4.23,

 "ronname_header": "RON",
 "ron [e-]": 6.01,

 "scalename_header": "SCALE",
 "scale": 0.322,

 "readaxisname_header": "READAXIS",
 "readaxis": "line",

 "radius_FOV [arcmin]": 5.9
 }
]
```

ASAS J052919-1617.4 physical parameters file


```
[
 {
 "binary_name": "ASASJ052919-1617.3",
 "ra": "05:29:19.347",
 "dec": "-16:17:18.4",
 "mag_binary (G)": 13.459,

 "period_AAVSO (d)": 0.660855,
 "perioderror_AAVSO (d)": 0.000010,
 "hjd_0 AAVSO (HJD)": 2451868.72,
 "hjd_0_error AAVSO (HJD)": 0.01,

 "period (d)": 0.66085103,
 "period_error (d)": 0.00000018,
 "hjd_0 (HJD)": 2459929.50048,
 "hjd_0_error (HJD)": 0.00021,

 "ra_comparison1": "05:29:28.468",
 "dec_comparison1": "-16:18:35.26",
 "mag_comparison1 (G)": 12.206,
 "ra_comparison2": "05:29:08.807",
 "dec_comparison2": "-16:18:14.81",
 "mag_comparison2 (G)": 13.122
 }
]
```


Teide Observatory parameters file


```
 [
  {
  "observatory": "OT",
  "longitude (deg)": -16.50972222,
  "latitude (deg)": 28.3,
  "elevation (m)": 2390,
  "timezone": "Europe/London"
}
 ]
```